Available online at www.sciencedirect.com
SCIENCE DIRECT®
Geochimica et Cosmochimica Acta 70 (2006) 901–917
Geochimica
www.elsevier.com/locate/gca

Evidence for the nucleation and epitaxial growth of Zn phyllosilicate on montmorillonite

Michel L. Schlegel [a,*], Alain Manceau [b]

[a] CEA, Laboratory for the Reactivity of Surfaces and Interfaces and UMR 8587, DANS/DPC/SCP/LRSI, CEN of Saclay, Bât. 391, F-91191 Gif-sur-Yvette Cedex, France
[b] Environmental Geochemistry Group, Maison des Géosciences, Université J. Fourier and CNRS, BP 53, F-38041 Grenoble Cedex 9, France

Received 25 March 2005; accepted in revised form 26 October 2005

Abstract

Zinc uptake in suspensions ($\leqslant$3.7 g L^{-1}) of MX80 montmorillonite was investigated at pH 4.0 and 7.3, a total Zn concentration ($[Zn]_{total}$) of 500 μM, and dissolved Si concentrations ($[Si]_{aq}$) of ~70 and ~500 μM in 0.5 M NaCl, by kinetics experiments and polarized extended X-ray absorption fine structure (P-EXAFS) spectroscopy. Differential thermogravimetric analysis verified the cis-vacant character of the montmorillonite. No Zn uptake occurred at pH 4.0, confirming that cation exchange was hampered by the high ionic strength of the suspension. At pH 7.3 and low $[Si]_{aq}$ (~70 μM), Zn uptake occurred rapidly during the first hour of reaction, and then leveled off to 50 μmol/g montmorillonite at 168 h. The uptake rate is consistent with Zn sorption on pH-dependent edge sites. At pH 7.3 and high $[Si]_{aq}$ (~500 μM), the initial sorption rate was similar, but Zn sorption continued, reaching 130 μmol/g at 168 h, and was paralleled by Si uptake with a Si/Zn uptake ratio of 1.51(10), suggesting formation of a Zn (hydrous) silicate. P-EXAFS data indicated that the first oxygen coordination shell of sorbed Zn is split into two subshells at 1.97(2) and 2.08(3)–2.12(2) Å for all EXAFS samples. These two distances are assigned to a mixture of tetrahedral (^{IV}Zn) and octahedral (^{VI}Zn) Zn complexes. The proportion of ^{IV}Zn was lower in the high $[Si]_{aq}$ samples and decreased with reaction time. Al low $[Si]_{aq}$ and 216 h of reaction, nearest cationic shells of 0.6(4) Al in the film plane and 0.5(4) Si out of the film plane were detected at 3.00(2) and 3.21(2) Å, respectively, and were interpreted as the formation of ^{IV}Zn and ^{VI}Zn mononuclear complexes at the edges of montmorillonite platelets, in structural continuity to the (Al, Mg) octahedral sheets. At high $[Si]_{aq}$, in-plane Zn and Al and out-of-plane Si neighbors were detected at 4 h, indicating the formation of Zn phyllosilicate nuclei at the layer edges. At 313 h, Zn–Al pairs were no longer detected, and Zn atoms were surrounded on average by 3.4(5) in-plane Zn at 3.10(1) Å and 1.7(9) out-of-plane Si at 3.30(2) Å, supporting the precipitation of a Zn phyllosilicate. Thus, dioctahedral Al phyllosilicate may act as a nucleating surface for the heterogeneous formation of trioctahedral Zn phyllosilicate at $[Si]_{aq}$ relevant to natural systems.

1. Introduction

Natural (bio)accumulation and anthropogenic activities can both result in locally high concentrations of trace elements, as in marine and terrestrial ferro-manganese nodules (Manceau et al., 2003; Marcus et al., 2004), or in polluted areas near smelters and waste disposals (Manceau et al., 1996, 2000; Morin et al., 1999; Webb et al., 2000; Scheinost et al., 2002). These (bio)geochemical enrichments generally persist as a result of element immobilization by inorganic solids. For example, field studies and batch experiments on bentonite powders outlined the importance of Zn retention by phyllosilicates, either by sorption on the surface or by incorporation in a clay structure (Ross, 1946; Manceau et al., 2000, 2002a, 2004; Scheinost et al., 2002; Lee et al., 2004; Isaure et al., 2005; Panfili et al., 2005). To better understand the physico-chemical conditions favoring either of these two retention mechanisms, characterization of the reactivity of soil phyllosilicates toward Zn and other trace elements is needed.

The molecular processes of cation uptake in purified clay systems have been investigated in detail, and the

* Corresponding author. Fax: +33 1 69 08 54 11.
E-mail address: Michel.Schlegel@cea.fr (M.L. Schlegel).

0016-7037/$ - see front matter © 2005 Elsevier Inc. All rights reserved.
doi:10.1016/j.gca.2005.10.021

sorbate binding environment identified in a number of studies by combining batch chemical, spectroscopic, and microscopic methods. Cation sorption by outer-sphere complexation, and neoformation of pure and mixed hydroxide phases, e.g., layered double hydroxides, have been observed by extended X-ray absorption fine structure (EXAFS) spectroscopy on powder and paste samples (Scheidegger et al., 1996, 1997; Manceau et al., 2002a; Scheinost et al., 2002; and references therein). Recent application of polarized EXAFS (P-EXAFS) spectroscopy proved essential to unambiguously identify specific sorption sites of trace elements on clay minerals (Schlegel et al., 1999b, 2001a,b; Dähn et al., 2001, 2002a,b, 2003). As an example, P-EXAFS was used to show that Zn-sorbed at moderate pH (6.5) on hectorite, a magnesian smectite, formed mononuclear complexes on the particle edges (see Fig. 1 in Schlegel et al., 2001a). This technique was further used to demonstrate that Zn phyllosilicate (Zn kerolite) can nucleate from these surface complexes, and grow epitaxially in only 5 days at near-neutral pH (7.3) and dissolved silicon concentrations ($[Si]_{aq}$) relevant to geochemical systems (Schlegel et al., 2001b). Nickel reacted with montmorillonite, the most common aluminum smectite in soils, bentonites, and sediments, was observed also to be incorporated in a neoformed phyllosilicate in two weeks at pH 8.0, but only after 1 year of reaction at pH 7.2 (Dähn et al., 2002a, 2003). The difference in reaction kinetics between the hectorite and montmorillonite experiments may simply reflect distinct chemical conditions, but it may also originate from differences in structural and chemical reactivity between the two systems (Güven, 1988). In hectorite, all sites of the octahedral sheet are filled with Mg, hence forming a trioctahedral framework, in which Zn can be easily incorporated (Decarreau, 1981b, 1985). In contrast, in montmorillonite, two-thirds of the octahedral sites are occupied mostly by Al and the other third is empty, yielding a dioctahedral framework. Divalent cations have a lower affinity for dioctahedral frameworks than for trioctahedral phyllosilicates, as suggested by the limited domain of solid solution between Mg and Al phyllosilicates (Grauby, 1993; Grauby et al., 1993). However, dioctahedral phyllosilicates are far more abundant than trioctahedral ones at the earth's surface and, consequently, may control the fate of divalent metals in the environment.

In this paper, the sorption mechanism of Zn on montmorillonite was investigated by solution chemistry and P-EXAFS spectroscopy. This study provides insight on the similarities and dissimilarities between the surface reactivity of magnesian and aluminum smectites.

2. Materials and methods

2.1. Montmorillonite

MX80 bentonite material was obtained from the French Agency for Management of Nuclear Waste (ANDRA). Twenty-five grams of raw bentonite was shaken in 1 L of bidistilled water (Milli-Q) for 2 days. The <2 μm montmorillonite fraction was isolated by centrifugation, and treated several times with a 0.1 M citrate, 0.5 M NaCl solution at pH 5 to remove carbonates, then with a dithionite–citrate–bicarbonate solution for 1 h at pH 6.5 to remove iron and manganese (oxyhydr)oxides, and finally with a 3% H_2O_2–0.5 M NaCl solution for 1 h at 50 °C to remove organic matter. The treated montmorillonite was repeatedly washed with 0.5 M NaCl and stored as a 4 wt % stock suspension in 0.5 M NaCl at 4 °C in the dark. The purified clay was characterized by X-ray diffraction on a Phillips X'Pert X-ray diffractometer. No mineral impurity was detected. The structural formula of the material as treated is $Na_{0.28}(Al_{1.61}Mg_{0.24}Fe^{3+}_{0.13}Fe^{2+}_{0.02})(Si_{3.98}Al_{0.02})O_{10}(OH)_2$, and the cation exchange capacity calculated from the clay composition equals 760 meq kg^{-1} (Tournassat et al., 2004). The specific surface area determined from morphological considerations equals 788 $m^2\ g^{-1}$ (Tournassat et al., 2003).

2.2. Differential thermal analysis

Thermal analysis was carried out with a Setsys 1600 analyzer (Setaram) in Ar atmosphere. About 70 mg of dried MX80 powder were loaded in an Al_2O_3 crucible. The sample was initially heated at 110 °C for 1 h, and then to 1000 °C at a rate of 5 °C/min.

2.3. Zn uptake experiments

All solutions were prepared with deionized water (Milli-Q or Elga Purelab UHQ) and chemicals of at least American Chemical Society reagent grade. Uptake experiments were performed in polyethylene vessels thermostated at 25.0 ± 0.1 °C (thereafter, the condensed notation 25.0(1) °C is used to express uncertainties). Suspensions were stirred with a magnetic bar, and an inert atmosphere was maintained by bubbling through the suspension a N_2 gas that was previously bubbled sequentially through 0.1 M NaOH, then 1 M H_2SO_4, and finally 0.5 M NaCl. A high Na concentration of 0.5 M was maintained using NaCl (Sigma) to prevent Zn adsorption on cation exchange sites of montmorillonite. pH values were measured with a combination micro-electrode (Mettler Todedo) calibrated with buffers (Merck, Titrisol), and recalibrated at least every 72 h. Suspension pH values were adjusted to, and maintained at, the desired pH by software-controlled addition of acidic (0.01 M HCl, 0.5 M NaCl), basic (0.02 M NaOH, 0.48 M NaCl), or basic silica (0.1 M SiO_2, 0.2 M NaOH, 0.3 M NaCl) solutions, according to experimental conditions.

Three experiments were performed to evaluate the impact of pH and $[Si]_{aq}$ on Zn uptake on montmorillonite. All three were conducted using 0.5 M NaCl solutions containing 3.7 g L^{-1} montmorillonite. For the first experiment (LoSi-4), the solution was adjusted to pH 4 using the acidic solution and equilibrated overnight by addition of the

acidic solution. In the second experiment (LoSi-7), the solution was adjusted to pH 7.3 and equilibrated overnight using the basic solution. No dissolved Si was added for LoSi-4 and LoSi-7, and therefore $[Si]_{aq}$ in these two suspensions resulted from montmorillonite dissolution only. In the third experiment (HiSi-7), the pH was adjusted to 7.3 and dissolved silica was added to obtain a concentration of ~500 μM using both the acidic and basic silica solutions. The solution was then equilibrated overnight.

For each uptake experiment, enough 0.2 M $ZnCl_2$ (pH 4.7) was added to obtain a total Zn concentration ($[Zn]_{total}$) of ~500 μM. After Zn addition, pH was adjusted to 4.00(5) (LoSi-4) or to 7.30(5) (LoSi-7 and HiSi-7) within 1 h and kept constant by adding acid (LoSi-4), basic silica (HiSi-7) or basic (LoSi-7) solutions at a slow rate (~60 μL min^{-1}) to minimize local supersaturation. At given times ($0 < t \leqslant 168$ h), 5 mL of suspension was pipetted from the reaction vessel with a pipette tip, centrifuged, and filtered (Whatman 0.1 μm cellulose nitrate filters). The first milliliter of the filtered supernatant was discarded to limit losses due to sorption on the filter. Solute Zn, Si, and Al concentrations in the filtered supernatant ($[Zn]_{aq}$, $[Si]_{aq}$, and $[Al]_{aq}$) were measured by inductively coupled plasma-atomic emission spectrometry (ICP-AES). $[Si]_{aq}$ never exceeded 600 μM, meaning that silicic acid was undersaturated with respect to amorphous silica and was predominantly monomeric (Iler, 1979; Stumm, 1992; Dietzel, 2000). Zn uptake was determined from the difference between $[Zn]_{total}$ and $[Zn]_{aq}$, taking into account the dilution caused by addition of basic or basic silica solutions (Schlegel et al., 2001b). Speciation calculations at $[Zn]_{aq} \leqslant 500$ μM showed that more than 98% of dissolved Zn was present as Zn_{aq}^{2+} (Baes and Mesmer, 1976). Calculation of saturation indices Ω (defined as the ratio of the ion activity product, IAP, to the solubility constant K_{eq}; Stumm and Morgan, 1996) using the Pitzer model in the $ZnCl_2$–HCl–NaCl mixture for activity coefficients (Pitzer, 1987, 1991) showed that $[Zn]_{aq}$ never reached the solubility limits of ZnO or $Zn(OH)_2$ (at $t = 0$, $\Omega_{ZnO} = (Zn^{2+})/[(H^+)^2 \cdot K_{eq}^{ZnO}] = 0.08$, and $\Omega_{Zn(OH)_2} = (Zn^{2+})/[(H^+)^2 \cdot K_{eq}^{Zn(OH)_2}] = 0.06$, where (Zn^{2+}) and (H^+) are the activities of Zn^{2+} and H^+ in solution; Baes and Mesmer, 1976). To our knowledge, no thermodynamic data on the formation of dissolved Zn–silicate complexes is available, and previous EXAFS data suggested that this complexation reaction is marginal under our experimental conditions, even at high $[Si]_{aq}$ (Schlegel et al., 2001b).

2.4. Sample preparation for EXAFS spectroscopy

Suspensions for EXAFS samples were prepared and reacted at pH 7.30(5) using the same protocol as for solution chemistry studies, except for the solid concentration in the "high" $[Si]_{aq}$ preparation, which was brought to a value of 0.5 g L^{-1} to favor the observation of long-term uptake products. Self-supporting films of Zn-sorbed montmorillonite were obtained by slowly filtering on 0.1 μm Millipore cellulose nitrate filters 60 mL of reacted suspensions withdrawn at $t = 216$ h (LoSi-7-X216h, where 'X' stands for X-ray probed sample), 4 h (HiSi-7-X4h), and 313 h (HiSi-7-X313h). Filtration was performed under a continuous flow of N_2 to limit contamination by atmospheric carbonate. Excess salt and aqueous Zn in the wet films were rinsed with a few milliliters of deionized water before drying. Previous studies have shown that highly textured self-supporting films are obtained with the same protocol (Manceau et al., 1998; Schlegel et al., 1999b, 2001b; Dähn et al., 2003). Several slices of each film were cut and stacked on a sample holder for EXAFS measurements. The names and the preparation conditions of the probed samples are given in Table 1.

Table 1
Samples reacted at pH 7.3 and analyzed by EXAFS spectroscopy

Sample names	[mont.][a] (g L^{-1})	Zn uptake[b] (%)	Γ[c] (μmol Zn g^{-1} montmorillonite)	$[Si]_{aq}$ (μM)	Time (h)
LoSi-7-X216h	3.7	37.5	51	~70	216
HiSi-7-X4h	0.5	28.4	52	548	4
HiSi-7-X313h	0.5	90.7	660	530	313

[a] Montmorillonite concentration in the suspension.
[b] Amount of $[Zn]_{total}$ adsorbed on montmorillonite.
[c] Zinc surface coverage.

2.5. EXAFS data collection and reduction

Zn K-edge EXAFS spectra were recorded at the European Synchrotron Radiation Facility (ESRF, France) on the FAME (BM30B) station. The spectrometer optics includes a Ni-coated focusing mirror and a sagittal-focusing, double crystal Si(111) monochromator (Hazemann et al., 1995). Clay films were mounted on a goniometer, and EXAFS spectra were recorded at $\alpha = 10°$, 35°, 55°, and 80° (where α is the angle between the phyllosilicate basal plane and the electric field vector of the linearly polarized X-ray beam). The most Zn concentrated sample (HiSi-7-X313h) was recorded in transmission mode, using photodiode detectors. The two other samples (HiSi-7-X4h and LoSi-7-X216h) were recorded in fluorescence detection mode, using a 30 element array Ge detector. The Arizona montmorillonite from the Source Clays Repository of the Clay Minerals Society (Zn-SAz) was used as a standard for Zn substituted for Al in the clay octahedral sheet. Its Zn K-edge EXAFS spectrum was collected in fluorescence mode on a pressed pellet oriented at the magic angle relative to the incoming beam (i.e., $\alpha = 35°$). At this angle, all potential texture effects arising from the anisometry of clay crystallites are cancelled, and P-EXAFS and powder EXAFS spectra are the same (Manceau et al., 1990). Other references included aqueous Zn (Zn_{aq}^{2+}), Zn kerolite ($Zn_3Si_4O_{10}(OH)_2 \cdot nH_2O$; ZnKer300), mixed (Zn,Mg) kerolite ($Zn_{1.35}Mg_{1.65}Si_4O_{10}(OH)_2 \cdot nH_2O$; ZnKer135), and Zn-sorbed on hectorite at pH 6.5 (Zn-hect). In all the solid references, Zn is located in a clay structural environment and bonded to in-plane Zn and Mg octahedra at 3.0–3.1 Å, and to out-of-plane Si tetrahedra at 3.2–3.3 Å, but the number and relative proportions of the neighboring Mg and Si cations

differ from one reference to another. In ZnKer300, Zn Ker135, and Zn-hect, Zn is surrounded by 6 Zn and 4 Si, by 2.7 Zn, 3.3 Mg, and 4 Si, and by 1.6 Mg and 2.7 Si, respectively (Manceau et al., 2000; Schlegel et al., 2001a).

EXAFS data were reduced with the SEDEM software (Aberdam, 1998). First, absorption spectra were given the shape of the Stobbe function, which is a quantum-mechanically derived formula for atomic absorption. Then standard fitting procedures were used to extract the EXAFS spectra ($\chi(k)$; Teo, 1986). Fourier transformations were performed on $k^3\chi(k)$ functions between $k = 2.5$ and 12 Å^{-1} using a Kaiser apodization window (Manceau and Combes, 1988). Fourier transforms (FTs) display amplitude maxima (peaks) located at apparent ($R + \Delta R$) distances which differ from the EXAFS path lengths (R) by $\Delta R \sim -0.3$ to -0.4 Å for $R < \sim 4$ Å (Teo, 1986). Peaks of interest were selected and fitted in the R-space with the Artemis interface to the IFEFFIT software (Newville et al., 1993; Newville, 2001; Ravel and Newville, 2005), using theoretical phase and amplitude functions calculated with FEFF7.02 (Ankudinov and Rehr, 1997), and Zn-doped montmorillonite as a model structure (Tsipursky and Drits, 1984). The amplitude reduction factor S_0^2 was set to 0.85 in agreement with previous studies (e.g., Schlegel et al., 2001b). All polarized spectra from the same sample were fit together using common values for ΔE_0 (the edge-shift between theoretical and experimental data), EXAFS distances ($R_{\text{Zn-j}}^{\text{EXAFS}}$), and Debye-Waller parameters (σ_j, accounting for static and thermal disorders) of the jth shell. The numbers of neighboring atoms (N^{α}) were fit independently for each α angle. The goodness of the fits was quantified by the R_{p} factor, defined as

$$R_{\text{p}} = \frac{\sum_{i=1}^{N}\left\{[\text{Re}(f_i)]^2 + [\text{Im}(f_i)]^2\right\}}{\sum_{i=1}^{N}\left\{[\text{Re}(\text{FT}_{\text{data}}(P_i))]^2 + [\text{Im}(\text{FT}_{\text{data}}(P_i))]^2\right\}}, \qquad (1)$$

where $\text{Re}(f_i)$ and $\text{Im}(f_i)$ are the real and imaginary parts of the difference function $f_i = [\text{FT}_{\text{data}}(P_i) - \text{FT}_{\text{model}}(P_i)]$, $\text{FT}_{\text{data}}(P_i)$ and $\text{FT}_{\text{model}}(P_i)$ are the FT functions of the experimental data and model, and the summation runs over all P_i values of the fitted $R + \Delta R$ range. Statistical uncertainties on the fitted parameters were calculated following standard procedures implemented in FEFFIT (Newville, 2001). The precision on EXAFS parameters is typically ±0.02 Å for $R_{\text{Zn–O}}^{\text{EXAFS}}$, $R_{\text{Zn–Zn}}^{\text{EXAFS}}$, $R_{\text{Zn–Al}}^{\text{EXAFS}}$, and $R_{\text{Zn–Si}}^{\text{EXAFS}}$, values that are similar to those previously reported (Schlegel et al., 2001a). Multiple scattering contributions to the total EXAFS spectra were not included in the fits because they were shown to be weak, especially in dioctahedral phyllosilicate (Manceau et al., 1998).

3. Results and interpretations

3.1. Differential thermal analysis

The differential thermal curve for MX80 displays an endothermic minimum at 670 °C, confirming the expected cis-vacant nature of the montmorillonite (Drits et al., 1995), as it is generally the case for Fe-poor dioctahedral smectites (Tsipursky and Drits, 1984).

3.2. Uptake kinetics

Previous experiments showed that in a solution containing $[\text{Si}]_{\text{aq}} \sim 500$ μM and $[\text{Zn}]_{\text{aq}} \sim 500$ μM, $[\text{Zn}]_{\text{aq}}$ remained constant, even after several days of reaction time (Schlegel et al., 2001b). The absence of Zn uptake precludes the formation of large amounts of homogeneous Zn precipitate. Zinc may have formed small nuclei that would not be separated from the supernatant upon centrifugation and filtration, but no such polymers were detected by EXAFS (Schlegel et al., 2001b). Consequently, the homogeneous nucleation of Zn–Si solids in our experimental conditions (pH 7.3, $[\text{Zn}]_{\text{total}} = 500$ μM, $[\text{Si}]_{\text{aq}} \sim 500$ μM) is negligible, if occurring at all, in the time span of our experiments.

No Zn uptake occurred in the LoSi-4 experiment, confirming that cation exchange was effectively hampered by the high ionic strength of the suspension. In contrast, Zn uptake occurred in the LoSi-7 and HiSi-7 experiments, supporting a pH-dependent sorption of Zn at the clay surface, probably on layer edges as previously observed on hectorite (Schlegel et al., 2001a; Fig. 1A). When no Si was added (LoSi-7), 33% of $[\text{Zn}]_{\text{total}}$ (44 μmol g^{-1} montmorillonite) was sorbed within the first hour, and Zn uptake progressed only slightly afterwards up to 37% of $[\text{Zn}]_{\text{total}}$ (50 μmol g^{-1} montmorillonite) at $t = 168$ h. The initial Zn sorption for HiSi-7 (46 μmol g^{-1} montmorillonite at $t = 1$ h) was similar to LoSi-7. Sorption in HiSi-7 continued afterwards, and nearly 96% of $[\text{Zn}]_{\text{total}}$ (130 μmol g^{-1} montmorillonite) was sorbed after 168 h of reaction.

The impact of Zn uptake on montmorillonite dissolution and $[\text{Si}]_{\text{aq}}$ variations was also examined. For the LoSi-7 experiment, $[\text{Si}]_{\text{aq}}$ remained nearly constant near ~70 μM (Fig. 1B), whereas $[\text{Al}]_{\text{aq}}$ hovered around the detection limit of ICP-AES (~0.2 μM). The at least two orders of magnitude difference between $[\text{Si}]_{\text{aq}}$ and $[\text{Al}]_{\text{aq}}$ contrasts with the Si/Al stoichiometric ratio in MX80 (Si/Al = 3.98/1.61 = 2.47). The low concentration of $[\text{Al}]_{\text{aq}}$ may be explained by the precipitation of Al polymers under the near-neutral pH condition of the suspension. Low amounts of $[\text{Al}]_{\text{aq}}$ (<0.4 μM) were also observed for HiSi-7. Although significant volumes of basic silica were added to the HiSi-7 suspension to keep the pH at 7.30, $[\text{Si}]_{\text{aq}}$ actually decreased with time (Fig. 1B), indicating that Si uptake occurred during Zn uptake. This is clearly apparent in Fig. 1C, which compares the measured values of $[\text{Si}]_{\text{aq}}$ to those calculated by assuming that all Si added with the basic silica solution had accumulated in the suspension. Interestingly, the ratio of the Si to Zn uptake is constant for $t \geqslant 4$ h (Fig. 1D) and equals 1.51(10), suggesting the formation of a well-defined Zn–Si solid phase. This ratio is too high for 2:1 layer (TOT) or 1:1 layer (TO) Zn phyllosilicates ($Zn_3Si_4O_{10}(OH)_2$ and $Zn_3Si_2O_5(OH)_4$, respectively). Polarized-EXAFS measurements were undertaken to

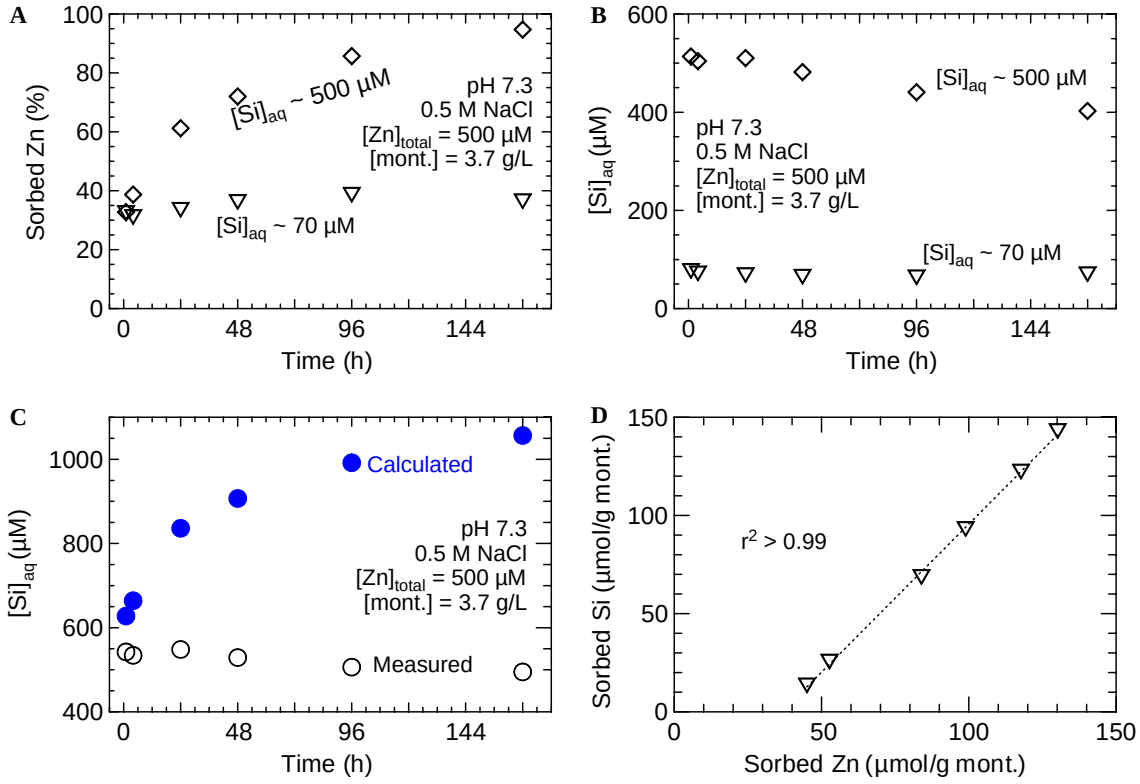

Fig. 1. (A) Zinc uptake as a function of time and $[Si]_{aq}$. $[Zn]_{total} = 500$ µM, montmorillonite concentration [mont.] = 3.7 g L^{-1}, and pH 7.3 for all experiments. The concentration uncertainty is smaller than the symbols. (◇): Zinc uptake for $[Si]_{aq} \sim 500$ µM, (HiSi-7 experiment); (▽): Zinc uptake for $[Si]_{aq} \sim 70$ µM (LoSi-7 experiment). (B) $[Si]_{aq}$ in the HiSi-7 experiment (◇), and in the LoSi-7 experiment (▽). (C) Comparison between $[Si]_{aq}$ measured in the HiSi-7 experiment (○), and theoretical $[Si]_{aq}$ values assuming accumulation of all added Si in the supernatant (●). (D) Plot of Si uptake versus Zn uptake for the HiSi-7 experiment. The slope of the regression line equals 1.51(10).

further examine the molecular mechanisms of Zn uptake with and without silica.

3.3. EXAFS spectroscopy

3.3.1. EXAFS spectra

The k^3-weighted P-EXAFS spectra for sorption samples all display a marked angular dependence of the amplitude and position of the EXAFS oscillations, e.g., near 5.2 and 6.0 $Å^{-1}$ (Fig. 2). This spectral dichroism suggests that Zn atoms are structurally connected to montmorillonite particles and confirms, a posteriori, the high texture strength of the self-supporting films. However, the P-EXAFS spectra for the three samples differ in oscillation amplitudes and angular dependency, demonstrating that the Zn binding environment varies from one sample to another (Fig. 2). The LoSi-7-X216h spectrum recorded at $\alpha = 35°$ is relatively featureless, differing only from the Zn_{aq}^{2+} spectrum by the presence of shoulders on the side of the EXAFS oscillations at 6.5 and 7.5 Å (Fig. 3). This suggests that Zn is not surrounded by many ordered atomic shells in LoSi-7-X216h. In contrast, HiSi-7-X313h resembles ZnKer300. Spectral features for HiSi-7-X4h are

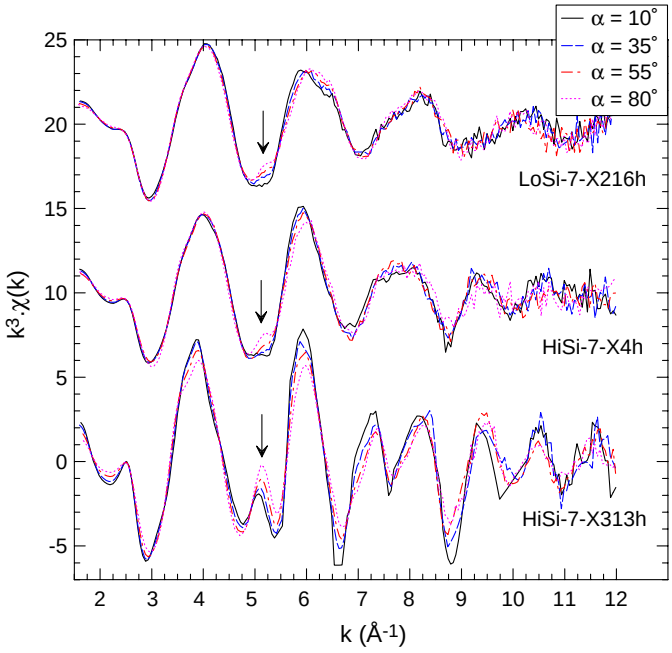

Fig. 2. k^3-weighted Zn K-edge P-EXAFS spectra for Zn-sorbed montmorillonite films at α angles of 10°, 35°, 55°, and 80°.

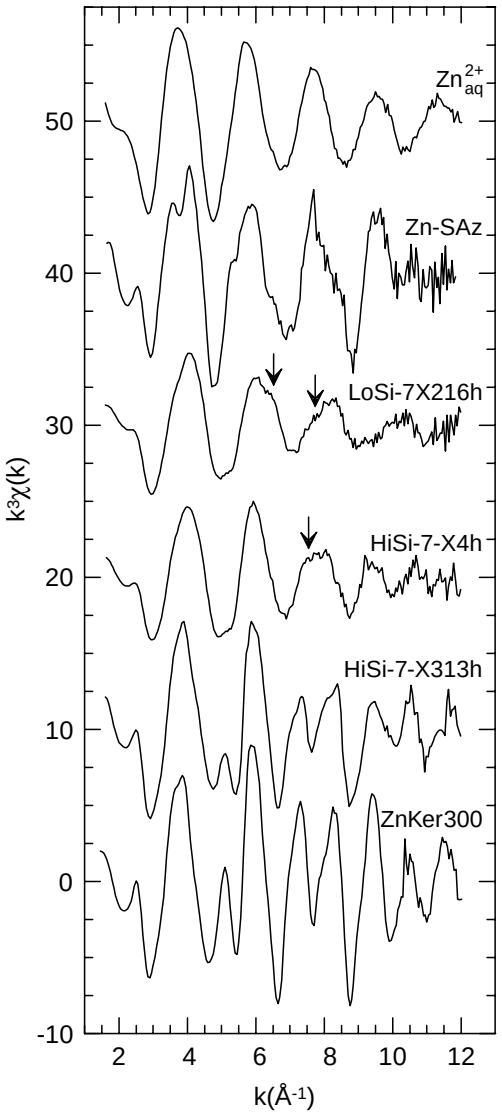

Fig. 3. k^3-weighted Zn K-edge EXAFS spectra for aqueous Zn (Zn$_{aq}^{2+}$), Zn-containing natural montmorillonite (Zn-SAz), Zn kerolite (ZnKer300), and Zn-sorbed montmorillonite films. All spectra were recorded at the magic angle ($\alpha = 35°$).

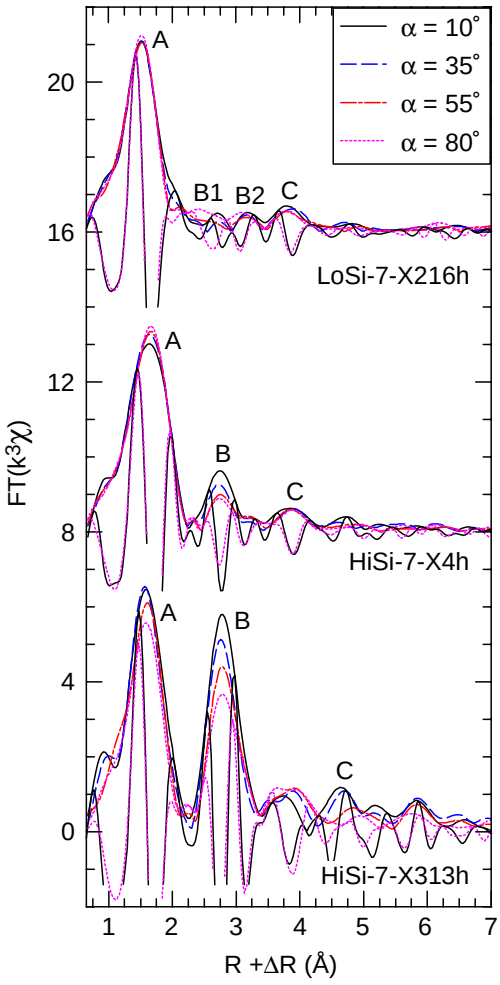

Fig. 4. Moduli of the Fourier transforms (|FT|s) for Zn-sorbed montmorillonite films at α angles of 10°, 35°, 55°, and 80°. The imaginary parts of the FTs are also plotted for $\alpha = 10°$ and 80°.

intermediate between those of LoSi-7-X216h and HiSi-7-X313h. This is the case for the 9.5 Å^{-1} oscillation, which is absent in LoSi-7-X216h, noticeable in HiSi-7-X4h, has a high amplitude in HiSi-7-X313h, and an even higher amplitude in ZnKer300. Also, the depth of the wave splitting at 7.5 Å^{-1} is shallower in HiSi-7-X313h than in ZnKer300, and is no longer observed in HiSi-7-X4h, though the third oscillation of this spectrum is clearly composite, in comparison to LoSi-7-X216h. Note that none of the sample spectra resembles Zn-SAz (Fig. 3), which allows one to dismiss the incorporation of Zn at Al sites in the bulk of MX80 octahedral sheets.

3.3.2. Fourier transforms

All Fourier transforms (FTs) display peaks at distances (uncorrected for phase shifts) of ~1.6 Å (peak A) and 3.8 Å (peak C) (Fig. 4). The HiSi-7-X4h and HiSi-7-X313h FTs also have a peak at 2.8 Å (peak B), whereas this peak B seems split into B1 and B2 in LoSi-7-X216h. The angular dependence of the moduli and imaginary parts of the Fourier transforms (|FT| and Im(FT), respectively) also shows the anisotropy of the Zn environment.

Plotting the Fourier back-transformed B1 and B2 contributions for LoSi-7-X216h over the [2.2, 3.5 Å] $R + \Delta R$ range against α angle (Fig. 5) shows that the weak amplitude of B1 and B2 results from cancellation effects of interfering EXAFS waves from different atomic shells. A similar cancellation effect was reported for Zn adsorbed to the edges of hectorite (Schlegel et al., 2001a). The position and amplitude of |FT|s and Im(FT)s in LoSi-7-X216h and Zn-hect bear strong resemblances, particularly in the $3 < R + \Delta R < 4$ Å interval (Fig. 6A′). Likewise, the FT of HiSi-7-X4h resembles the ZnKer135 reference from 2 to 4 Å, and HiSi-7-X313h the ZnKer300 reference over the same range (Figs. 6B′ and C′). These similarities between samples and references support the progressive incorporation of Zn in the octahedral sheet of a phyllosilicate structure along the sample series. With respect to the Zn local environment in phyllosilicate, we conclude that Zn

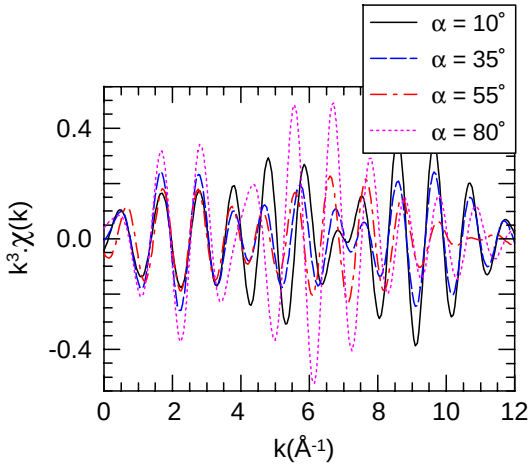

Fig. 5. Fourier-filtered EXAFS contributions for LoSi-7-X216h in the [2.2, 3.5 Å] interval.

is surrounded by (Si,Al) atoms at $R \sim 3.2$–3.3 Å in the out-of-plane direction, and by (Zn, Mg, or Al) atoms at $R \sim 3.0$–3.1 Å in the in-plane direction. In the following, peaks A, B, and C are analyzed successively.

Peak A originates from the contribution of oxygen atoms ligated to Zn. The position of |FT| and Im(FT) depend on the Zn–O distance, which in turn depends on the number of oxygen atoms coordinated to Zn (Kuzmin et al., 1997; Sarret et al., 1998). This is illustrated in Fig. 7A with ZnO, in which Zn is tetrahedrally coordinated (^{IV}Zn) with a Zn–O distance of ~1.96 Å, and with ZnKer300, in which Zn is octahedrally coordinated (^{VI}Zn) with a Zn–O distance of 2.06 Å. The Im(FT) plot for LoSi-7-X216h is close to that of ZnO on the short distance side of the FT peak, and to that of ZnKer300 on the high distance side. This suggests that both short and long Zn–O distances may be present in this sample. This inference was confirmed by least-squares fitting of the data, which

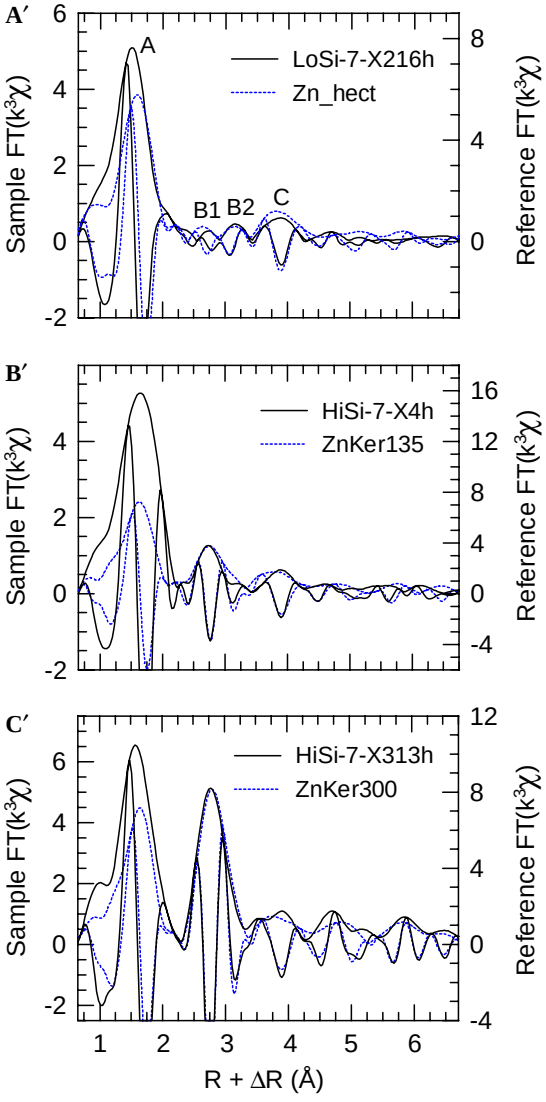

Fig. 6. Comparison of k^3-weighted FTs (moduli and imaginary parts) at the magic angle ($\alpha = 35°$) for LoSi-7-X216h and Zn-sorbed on hectorite (Zn-hect) (A′), HiSi-7-X4h and ZnKer135 (B′), and HiSi-7-X313h and ZnKer300 (C′).

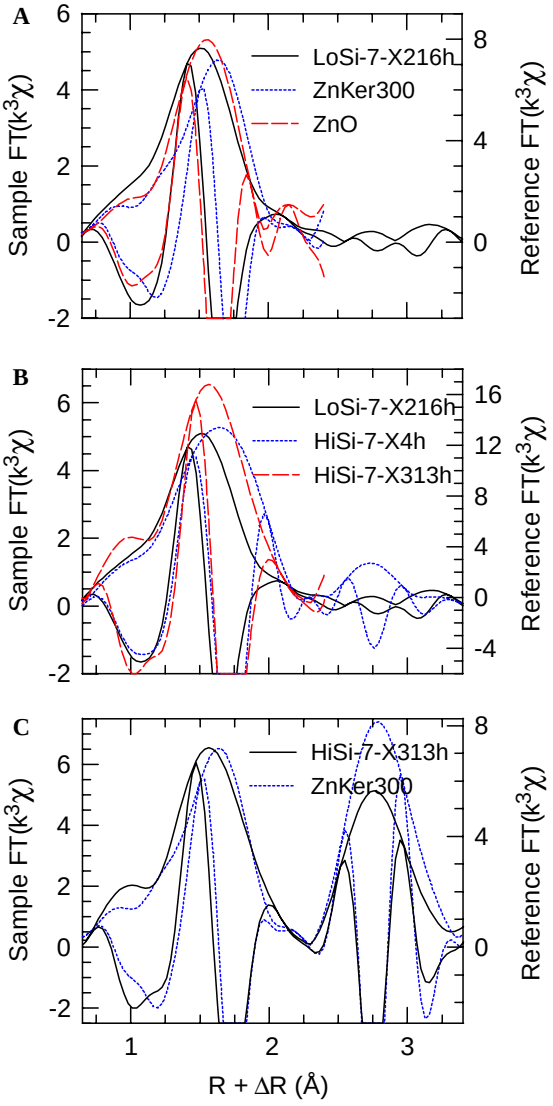

Fig. 7. Comparison of k^3-weighted FTs in the [0.7, 3.4 Å] interval (peak A) for LoSi-7-X216h, ZnKer300, and ZnO (A); LoSi-7-X216h, HiSi-7-X4h, and HiSi-7-X313h (B); and HiSi-7-X313h and ZnKer300 (C).

Table 2
Quantitative EXAFS analysis of the Zn–O coordination shell

Samples	α	Fit range[a] (Å)	$R^{EXAFS}_{Zn-O_{1A}}$ (Å)	$N_{O_{1A}}$	σ (Å)	$R^{EXAFS}_{Zn-O_{1B}}$ (Å)	$N_{O_{1B}}$	σ (Å)	ΔE_0[b] (eV)	R_P[c]
LoSi-7-X216h	10°	1.1–2.2	1.97(2)	3.9(3)	0.083	2.12(2)	2.5(2)	0.083	5.3	0.004
	35°	1.0–2.2		4.0(3)			2.2(2)			0.002
	55°	1.0–2.2		4.0(3)			1.9(3)			0.005
	80°	1.1–2.2		4.1(3)			1.7(3)			0.003
HiSi-7-X4h	10°	1.1–2.2	1.97(2)	2.3(3)	0.067	2.12(2)	3.6(4)	0.067	5.3	0.020
	35°	1.1–2.2		2.2(4)			4.0(4)			0.016
	55°	1.1–2.2		2.2(4)			3.9(4)			0.016
	80°	1.1–2.2		2.5(4)			3.3(5)			0.012
HiSi-7-X313h	10°	1.2–2.2	1.96(3)	3.2(5)	0.094	2.08(3)	5.7(5)	0.094	2.1	0.032
	35°	1.2–2.2		2.5(5)			5.4(5)			0.020
	55°	1.2–2.2		1.9(5)			5.6(5)			0.003
	80°	1.1–2.2		1.5(5)			5.1(5)			0.004

[a] $R + \Delta R$ interval for the fit in the real space.
[b] Threshold energy E_0 taken at the half-height of the absorption edge ($\Delta\mu/2$).
[c] Figure of merit of the fit.

yielded two oxygen subshells (O_{1A} and O_{1B}) at $R^{EXAFS}_{Zn-O_{1A}} = 1.97(2)$ and $R^{EXAFS}_{Zn-O_{1B}} = 2.12(2)$ Å ($\sigma = 0.08(3)$ Å; Table 2). The existence of two distances may arise from a distortion of the Zn coordination polyhedron, due to Zn–ligand bonds with contrasted bond strengths, or from a mixture of ^{IV}Zn and ^{VI}Zn species. In the first case, some Zn–O bonds should be shorter, some Zn–O bonds longer, and the average bond length longer than in an undistorted polyhedron (Brown, 1992). Here, the attribution of $R^{EXAFS}_{Zn-O_{1A}}$ and $R^{EXAFS}_{Zn-O_{1B}}$ values to short and long Zn–O bonds from the same octahedron is questionable, because the average $R^{EXAFS}_{Zn-O_1} = 2.04$ Å is apparently shorter than for an undistorted Zn octahedron (2.06 Å; Manceau et al., 2002b). Additional argument against the attribution of $R^{EXAFS}_{Zn-O_{1A}}$ to short bonds in a distorted octahedron is provided by the calculation of the theoretical length of the long $R^{EXAFS}_{Zn-O_{1B}}$ bonds needed to balance the Zn valence if $R^{EXAFS}_{Zn-O_{1A}} = 1.97$ Å. According to the bond valence-bond distance correlation function for oxygen and a cation M (Brown, 1981, 1992),

$$v_{M-O} = \exp\left(\frac{R^0_{M-O} - R_{M-O}}{0.37}\right), \quad (2)$$

where R_{M-O} is the cation to oxygen distance, and $R^0_{M\text{-}O}$ a tabulated empirical parameter (Brese and O'Keeffe, 1991), the bond valence associated with $R^{EXAFS}_{Zn-O_{1A}} = 1.97(2)$ Å is $v_{Zn-O_{1A}} = 0.49(3)$ valence units (v.u.). The average distance of the long bonds can be deduced from the valence sum rule (Brown, 1992), which states that the sum of bond valences incident to any cation M should equal the cation valence V_M, i.e.,

$$V_M = \sum_j v_{M-Oj}. \quad (3)$$

Since $N^{\alpha}_{O_{1A}} \geqslant N^{\alpha}_{O_{1B}}$ at all α angles in LoSi-7-X216h, a minimum of three short bonds for each distorted octahedron is expected. Then, to satisfy Eq. (3) with $V_{Zn} = 2$, the valence of the long Zn–O bond should be $(2 - 3 \times 0.49(3))/3 = 0.18(3)$ v.u. which imposes a Zn–O distance of 2.34(6) Å according to Eq. (2). This bond length is unrealistically long and clearly off the experimental $R^{EXAFS}_{Zn-O_{1B}}$ value. Likewise, the assumption of a distorted tetrahedral coordination can be ruled out for two reasons. First, Zn tetrahedra are less distorted than Zn octahedra (Sarret et al., 1998) and, second, tetrahedra distortion would result in Zn–O distances shorter than $R^{EXAFS}_{Zn-O_{1A}} = 1.97$ Å. Therefore, the $R^{EXAFS}_{Zn-O_{1A}} = 1.97(2)$ Å distance is assigned to ^{IV}Zn, and the $R^{EXAFS}_{Zn-O_{1B}} = 2.12(2)$ Å distance to ^{VI}Zn. Note however that the $R^{EXAFS}_{Zn-O_{1B}}$ value (2.12 Å) is greater than for an undistorted octahedron, which suggests that ^{VI}Zn octahedra are distorted.

At high $[Si]_{aq}$ and with increasing reaction time, Im(FT) for peak A gradually shifts to greater distances, but never coincides with that of ZnKer300, in which only ^{VI}Zn occurs (Figs. 7B and C). This indicates a progressive decrease of the ^{IV}Zn/^{VI}Zn ratio from LoSi-7-X216h to HiSi-7-X4h and to HiSi-7-X313h. This evolution along the sample series was confirmed by quantitative analysis, as the $N^{\alpha}_{O_{1A}}/N^{\alpha}_{O_{1B}}$ ratio was found to decrease at all α angles (Table 2). However, ^{IV}Zn did not disappear completely at high $[Si]_{aq}$ and reaction time, as apparent from the overplot of Im(FT) for HiSi-7-X313h and ZnKer300 (Fig. 7C). The $R^{EXAFS}_{Zn-O_{1A}}$ value is about invariant in the three samples, but $R^{EXAFS}_{Zn-O_{1B}}$ slightly decreases from 2.12(2) Å in HiSi-7-X4h to 2.08(3) Å in HiSi-7-X313h (Table 2). This reduction in $Zn–O_{1B}$ distance may result from a diminution of the distortion of the ^{VI}Zn octahedron, an hypothesis that will be discussed later.

Peak B (or B1 and B2 for LoSi-7-X216h) results from the interferences of the EXAFS contributions (χ_{Oct} and χ_{Tet}) from the nearest cationic shells in the octahedral (Oct) and tetrahedral (Tet) sheets, respectively (Manceau et al., 1998; Schlegel et al., 2001a). These interferences diversely affect the amplitude and position of peak B, depending on the nature and effective number of Oct and Tet cations in each shell. For example, the invariance in

phase and position of peak B with α for HiSi-7-X313h (Fig. 4) indicates that the χ_{Oct} and χ_{Tet} waves are essentially in-phase, as typically observed when the X-ray absorber (here Zn) is surrounded predominantly by 'heavy' atoms (e.g., Zn and Fe) in the octahedral sheet and 'light' atoms (e.g., Si, Al) in the adjacent tetrahedral sheets (Manceau et al., 1998; Schlegel et al., 2001b). In contrast, the B1 and B2 features for LoSi-7-X216h decrease in amplitude when α increases from $\alpha = 10°$ to 35°, and then increase in amplitude and are shifted to shorter $R + \Delta R$ distances when α increases to 80° (Fig. 4). A similar, though more pronounced, angular dependence was observed for Zn-hect, and was interpreted by a destructive interference between the χ_{Oct} and χ_{Tet} waves originating from 'light' in-plane Mg and out-of-plane Si atoms (see Fig. 11 in Schlegel et al., 2001a). The same explanation holds for LoSi-7-X216h, except that Al, instead of Mg, predominates in the montmorillonite octahedral sheet. This result supports the formation of Zn complexes at the edges of montmorillonite particles. Finally, the amplitude of peak B for HiSi-7-X4h is lower than that of HiSi-7-X313h at all α angles, and its Im(FT) slightly shifted with α (Fig. 7B). This finding, together with the similarity between HiSi-7-X4h and ZnKer135 data, are consistent with Zn being surrounded by a mixture of 'light' (Al, Mg) and 'heavy' (Zn, Fe) atoms in the plane of the octahedral sheet.

Peak B was best fitted with an Al shell at $R^{EXAFS}_{Zn-Al} = 3.00(2)$ Å and a Si shell at $R^{EXAFS}_{Zn-Si} = 3.21(2)$ Å ($\sigma_{Al} = \sigma_{Si} = 0.10$ Å) for LoSi-7-X216h, and with a Zn shell at $R^{EXAFS}_{Zn-Zn} = 3.10(2)$ Å and a Si shell at $R^{EXAFS}_{Zn-O_{Si}} = 3.30(2)$ Å ($\sigma_{Zn} = 0.096$ Å and $\sigma_{Si} = 0.084$ Å) for HiSi-7-X313h (Fig. 8 and Table 3). Since Zn is surrounded by octahedral Zn and Al in HiSi-7-X4h, the degree of freedom of the simulation is higher in this sample, and it was reduced by constraining R^{EXAFS} and σ values to be identical in the Zn and Al subshells. Optimal fits were obtained with $R^{EXAFS}_{Zn-Al} = R^{EXAFS}_{Zn-Zn} = 3.10(2)$ Å, $R^{EXAFS}_{Zn-Si} = 3.30(2)$ Å, $\sigma_{Al} = \sigma_{Zn} = 0.096$ Å and $\sigma_{Si} = 0.083$ Å (Fig. 8 and Table 3). The R^{EXAFS}_{Zn-Al}, R^{EXAFS}_{Zn-Zn} and R^{EXAFS}_{Zn-Si} values in all sorption samples are similar to those previously reported for ^{VI}Zn forming edge-sharing linkages with (Zn, Mg, Al) octahedra, and corner-sharing linkages with Si tetrahedra in phyllosilicates (Schlegel et al., 2001a,b; Manceau et al., 2005). However, the strongest argument in support of the phyllosilicate-like environment is given by the polarization dependence of the two nearest metal shells. In all samples, N^{α}_{Al} and N^{α}_{Zn} decreased with increasing α, implying that the Zn–Al and Zn–Zn pairs are oriented at β_{Al} and β_{Zn} angles > 54.7° with respect to the normal to the phyllosilicate layer (54.7° is the β magic angle, for which no angular dependence is observed; Manceau et al., 1988), whereas N^{α}_{Si} systematically increased

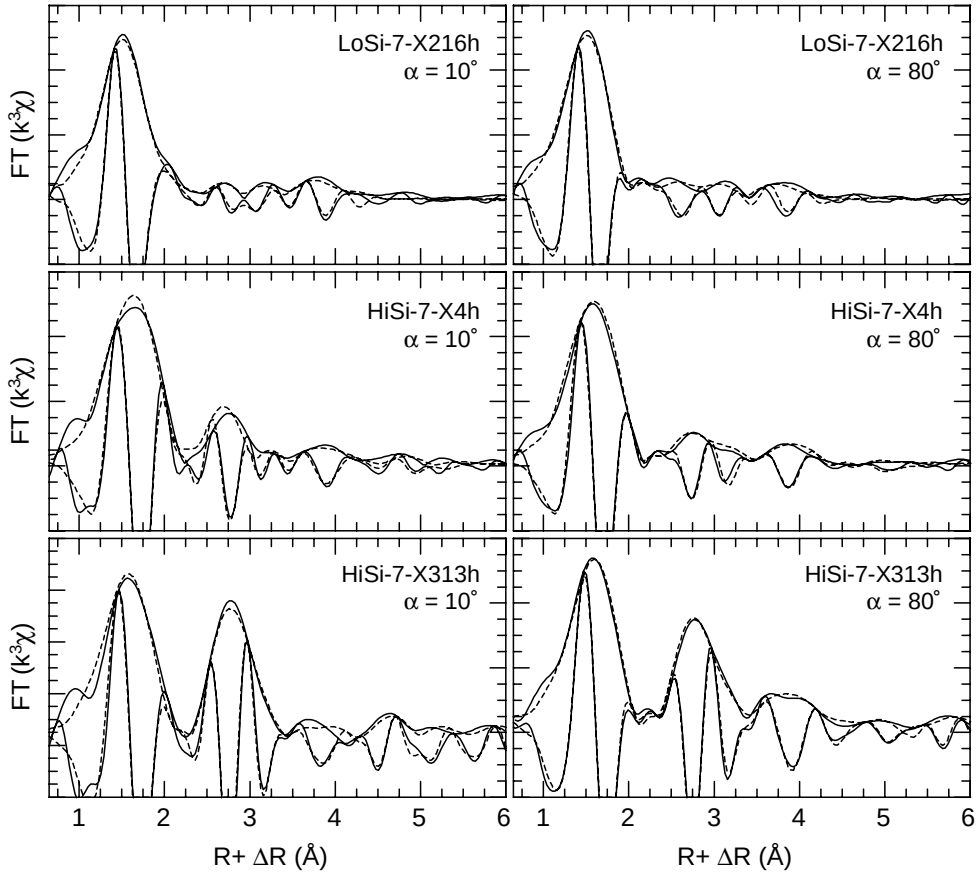

Fig. 8. Comparison of FT moduli and imaginary parts for the data (solid line) and spectral simulations (dotted lines). Left: $\alpha = 10°$. Right: $\alpha = 80°$.

Table 3
Quantitative EXAFS analysis of the nearest cationic shells

Samples	α	Fit range[a] (Å)	Zn–Al shell			Zn–Zn shell			Zn–Si shell			ΔE_0[b] (eV)	R_P
			R^{EXAFS}_{Zn-Al} (Å)	N_{Al}	σ (Å)	R^{EXAFS}_{Zn-Zn} (Å)	N_{Zn}	σ (Å)	R^{EXAFS}_{Zn-Si} (Å)	N_{Si}	σ (Å)		
LoSi-7-X216h	10°	1.1–3.4	3.00(2)	0.8(3)	0.10				3.21(2)	0.2(4)	0.10	5.3	0.006
	35°	1.1–3.4		0.6(4)						0.5(4)			0.003
	55°	1.1–3.4		0.3(5)						0.7(5)			0.006
	80°	1.1–3.4		0.0(5)						1.1(3)			0.004
HiSi-7-X4h	10°	1.1–3.5	3.10(2)[c]	1.9(5)	0.096[d]	3.10(2)[c]	1.9(3)	0.096[d]	3.30(2)	0.9(5)	0.084	5.3	0.022
	35°	1.1–3.4		1.2(5)			1.2(3)			1.2(5)			0.018
	55°	1.1–3.4		0.5(6)			0.7(3)			1.5(4)			0.017
	0°	1.1–3.4		0.0(8)			0.0(4)			2.6(5)			0.010
HiSi-7-X313h	10°	1.1–3.4				3.10(1)	4.3(6)	0.096	3.30(2)	1.4(1.0)	0.084	2.1	0.023
	35°	1.1–3.4					3.4(5)			1.7(9)			0.034
	55°	1.1–3.4					2.5(5)			2.0(8)			0.006
	80°	1.1–3.4					1.6(7)			3.0(9)			0.006

[a] $R + \Delta R$ interval for the fit in the real space. The fit was performed with oxygen and ΔE_0 parameters set at their values in Table 2.
[b] Threshold energy E_0 taken at the half-height of the absorption edge (Δμ/2).
[c] Distances were constrained to be identical for the Zn–Zn and Zn–Al pairs.
[d] σ values were constrained to be identical for Zn–Zn and Zn–Al pairs.

with α, meaning that $\beta_{Si} < 54.7°$, as in phyllosilicate structures (Fig. 1; Table 3).

Peak C in phyllosilicates originates from the contribution of next-nearest O and Si shells at ~4.2 and ~4.4–4.5 Å, respectively (Manceau et al., 1998). The systematic detection of these higher shells, in combination with the presence of Oct and Tet shells (peak B), indicates that the Si tetrahedra located near Zn atoms are polymerized in a two-dimensional framework linked to an octahedral sheet, as in a phyllosilicate (Fig. 6). The somewhat lower amplitude of peak C in the sorption samples, relative to ZnKer300, may result either from a higher structural disorder (i.e., high amount of defects) or from a lower amount of Si atoms near Zn (i.e., finite size of the Zn-containing nuclei) (Fig. 6). These EXAFS contributions were modeled by optimizing the number of O and Si atoms at this distance, and constraining their effective N^{α} values to vary with α as predicted by theory for Zn in phyllosilicate structures. This procedure yielded fair to good fits with fractional site occupancies of about 0.5, and R^{EXAFS} values differing by less than 0.2 Å from values calculated for Zn in a clay structure.

4. Discussion

4.1. Zn sorption at low $[Si]_{aq}$

4.1.1. Zn sorption sites at low $[Si]_{aq}$

At low $[Si]_{aq}$, most Zn uptake occurred within the first hour of contact time. Similar kinetics were observed previously for Zn sorbed as inner-sphere complexes on the edge sites of hectorite at high ionic strength (Schlegel et al., 2001b). After 216 h of contact time, both ^{IV}Zn and ^{VI}Zn were present on the montmorillonite surface and surrounded by an in-plane Al shell at $R^{EXAFS}_{Zn-Al} = 3.00(2)$ Å and an out-of-plane Si shell at $R^{EXAFS}_{Zn-Si} = 3.21(2)$ Å, as in phyllosilicate structures. This result is consistent with Zn located in structural continuity to the octahedral sheet of montmorillonite particles. Additional support for this interpretation comes from the detection of a next-nearest Si shell at ~4.4–4.5 Å, which is diagnostic of Zn bonded to a silica sheet (Manceau et al., 2000; Schlegel et al., 2001b). Note that the Zn binding environment described here differs from that in (Zn, Al) layered double hydroxide (Ford and Sparks, 2000).

More insight into the retention mechanism of Zn is provided from the number of nearest cations in the octahedral $[N_{Oct} \approx N^{35°}_{Al} = 0.6(4)]$ and tetrahedral $[N_{Tet} \approx N^{35°}_{Si} = 0.5(4)]$ sheets. These numbers are incompatible with a Zn for Al substitution in the montmorillonite structure, as in this case $N_{Oct} = 3$ and $N_{Tet} = 4$, or with Zn incorporation at vacant cis sites, as in this case $N_{Oct} = 6$. Therefore, Zn incorporation in the bulk montmorillonite layer is ruled out, leaving edge adsorption as the only plausible mechanism of Zn retention. The R^{EXAFS}_{Zn-Al} and R^{EXAFS}_{Zn-Si} values are shorter by 0.03 and 0.09 Å, respectively, than the R^{EXAFS}_{Zn-Mg} and R^{EXAFS}_{Zn-Si} values reported for ^{VI}Zn-sorbed on the edges of hectorite (Schlegel et al., 2001a). The decrease in distance may be explained by the smaller size of ^{IV}Zn (0.60 Å) relative to ^{VI}Zn (0.745 Å), and of $^{VI}Al^{3+}$ (0.535 Å) relative to $^{VI}Mg^{2+}$ (0.72 Å; Shannon, 1976). In conclusion, EXAFS results all collectively support the formation of inner-sphere Zn complexes at the edges of montmorillonite particles.

The structural characteristics of the particle edges and of edge sites can be inferred from morphological, crystallographic, and theoretical considerations (White and Zelazny, 1988; Bickmore et al., 2003; Tournassat et al., 2003). Atomic force microscopy revealed that the MX80 particles have an irregular 'corn-flake'-like morphology with no preferential crystallographic orientations of the layer edges (Tournassat et al., 2003). In the absence of well-developed lateral crystallographic faces, the possible

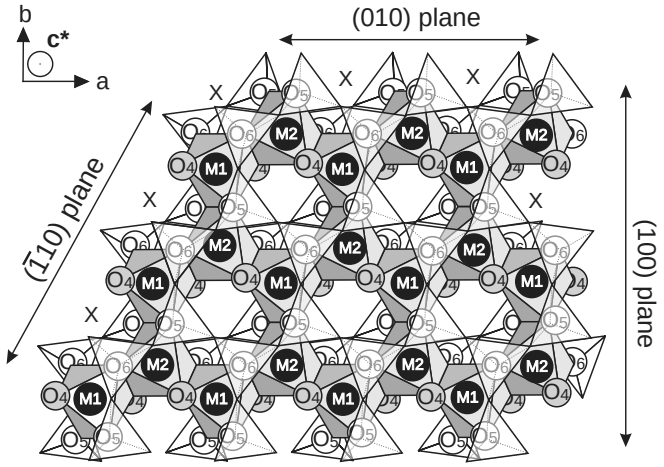

Fig. 9. Projection of the montmorillonite TOT structure in the ab plane, with emphasis on the schematic structure of layer edges. The faces from tetrahedra of the upper sheet are open for clarity. M1, trans sites; M2, cis sites.

structural terminations of the layer edges may be rationalized by interrupting the octahedral and tetrahedral sheets in such a way as to minimize the truncation energy (e.g., by breaking the weakest bonds or the minimum number of bonds; Bleam et al., 1993; Schlegel et al., 1999a; Bickmore et al., 2003). Several configurations for the (100), ($\bar{1}$10), and (010) faces can be obtained (Fig. 9). Note that only one cation-oxygen bond per surface oxygen is broken to obtain these surfaces. The strength of these broken bonds can be estimated from the montmorillonite crystallographic structure (Tsipursky and Drits, 1984; Fig. 9). Since MX80 montmorillonite has a cis-vacant structure, octahedral cations are theoretically evenly distributed between the trans M1 site and the cis M2 site (Fig. 9). However, according to Tsipursky and Drits (1984), the M1 site has a smaller size than the M2 and, thus, preferentially accommodates smaller cations, e.g., Al^{3+}, the M2 site being filled with Fe, Mg, and the remaining Al cations. The formal valence of the M2 site, derived from the chemical composition and the inferred site occupancy, is 2.74. On the basis of these crystallographic considerations, the bond valence of all atomic pairs in the structure and the valence of broken bonds for surface oxygens can be calculated. For this calculation, the valence of bonds incident to the M2 sites were calculated as the weighted sum of bond valences for Al, Mg, Fe(III), and Fe(II) present at this site (Brese and O'Keeffe, 1991). Results reported in Table 4 indicate that the valence of broken bonds for surface oxygens from the octahedral sheet (O4, O5, and O6) and tetrahedral sheet (O1, O2, and O3) are ~0.4–0.6 v.u. and ~0.9–1.1 v.u., respectively.

By analogy with Eq. (3),

$$V_O = \sum_j v_{Mj-O} \quad (4)$$

should be verified for surface oxygens, meaning that the deficit of v_{M-O} due to the breaking of structural bonds at the mineral surface should be balanced by protonation ($v_{H-O} \sim 0.8$ to 1 v.u.), formation of weak hydrogen bonds ($v_{H-O} \leqslant 0.2$), shortening of the remaining structural bonds, or the formation of new bonds, e.g., by adsorption of ^{IV}Zn ($v_{Zn-O} = 0.50$ v.u.), ^{VI}Zn ($v_{Zn-O} = 0.33$ v.u.), or distorted ^{VI}Zn ($0.33 < v_{Zn-O} < 0.4$ v.u.). As seen in Fig. 10, sorbate cations can be bound to O_{Oct} (i.e., O4, O5, and O6) and share one edge (E) with (Al, Mg) octahedra, and zero to two corners (C) with Si tetrahedra. The theoretical number of edge linkages (1.0) agrees with the experimental N_{Oct} value of 0.6(4), within uncertainty. Also, the $N_{Tet} = 0.5(4)$ value is consistent with an admixture of 50% S_{1E+0C} and 50% S_{1E+1C} surface complexes. Fig. 10 also shows that most surface complexes cannot share edges with each other. This situation stands in contrast to hectorite, in which adjacent surface complexes may exist owing to the trioctahedral nature of the octahedral sheet (Schlegel et al., 1999a). This structural difference likely accounts for the absence of Zn–Zn pairs on montmorillonite at low $[Si]_{aq}$, whereas some were detected on hectorite under

Table 4
Bond-valence values of layer atoms for K-montmorillonite

Central atom	Bonded atom	Bond valence	Sum	Formal valence
M1	2 × O4	2 × 0.53(4)	2.9(2)	3.00
	2 × O5	2 × 0.55(4)		
	2 × O6	2 × 0.38(3)		
M2	2 × O4	2 × 0.39(4)	2.7(2)	2.74
	2 × O5	2 × 0.49(4)		
	2 × O6	2 × 0.49(3)		
Si1	O1	1.04(5)	4.0(2)	4.00
	O2	0.98(5)		
	O3	0.98(5)		
	O6	1.01(5)		
Si2	O1	0.97(5)	4.0(2)	4.00
	O2	0.85(5)		
	O3	1.14(5)		
	O5	1.02(5)		
O1	Si1	1.04(5)	2.00(10)	2.00
	Si2	0.97(5)		
O2	Si1	0.98(5)	1.83(10)[a]	2.00
	Si2	0.85(5)		
O3	Si1	0.98(5)	2.12(10)	2.00
	Si2	1.14(5)		
O4	H[b]	1.00	1.92(8)	2.00
	M1	0.53(4)		
	M2	0.39(4)		
O5	Si2	1.02(5)	2.06(13)	2.00
	M1	0.55(4)		
	M2	0.49(4)		
O6	Si1	1.01(5)	1.88(11)	2.00
	M1	0.38(3)		
	M2	0.49(3)		

[a] The deficit in valence for O2 reflects the absence in the structural model of interlayer cations that transfer positive charge to basal oxygens.
[b] The bond valence for the O–H bond was set to 1.00 v.u., for consistency with previous studies on clay minerals (Manceau et al., 1998).

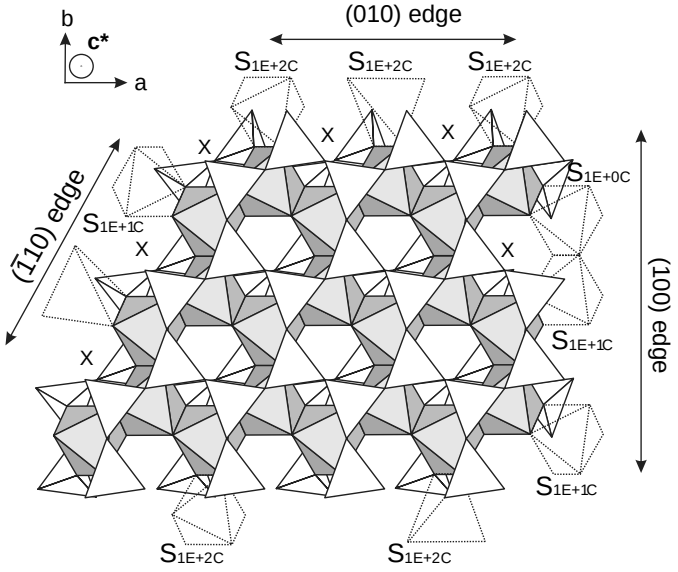

Fig. 10. Structural model of Zn sorption on montmorillonite at $[Si]_{aq} \sim 70$ μM and 216 h of reaction time (LoSi-7-X216h). In these conditions, Zn atoms form monomers on the edges. The letter 'X' marks visualize the center of some vacant octahedral sites.

comparable conditions of pH (7.3) and $[Si]_{aq}$ (~30 μM; Schlegel et al., 2001b). The absence of detected Zn–Fe pairs is consistent with the low amount of structural Fe octahedra statistically exposed at the surface (7.5%).

The particle edges also have vacant octahedra exposed to the solution, which might be filled by sorbate cations (Fig. 9). However, these octahedral sites are unlikely to be reactive because the inner oxygens are coordinated as in the bulk structure and, thus, do not require extra binding, except if a surface relaxation occurs. Note, however, that such relaxation would lead to the formation of 4E + 4C complexes, in contradiction with experimental N_{Tet} and N_{Oct} values.

4.1.2. Zn coordination by oxygen at low $[Si]_{aq}$

A coexistence of ^{IV}Zn and ^{VI}Zn surface species was also reported on Al_2O_3 from pH 5.1 to 8.2 (Trainor et al., 2000; Roberts et al., 2003). That dissolved Zn is in octahedral coordination under our experimental conditions (Waychunas et al., 2002) suggests that ^{IV}Zn formed on the clay surface, this coordination being possibly favored over ^{VI}Zn due to the good match between $v_{IV_{Zn-O}}$ (0.5 v.u.) and the valence of the surface broken bonds (~0.5 v.u.). However, the ^{VI}Zn complex may be stabilized by formation of hydrogen bonds between water molecules and surface oxygens. Assuming that not all surface oxygens form hydrogen bonds, this explanation may account for the coexistence of ^{IV}Zn and ^{VI}Zn surface species. ^{VI}Zn may also be stabilized at the M2 site by the presence of Al. If we assume that all the M2 sites have the same size, regardless of their Fe, Mg or Al occupancy, then their bigger size relative to M1 results in an undersaturation of the Al atoms at M2, in an amount equal to $V_{Al} - \sum_j v_{Al-Oj} = 3.0 - 2.6 = 0.4$ v.u.

This deficit in bond valence can be compensated by shortening the distance between Al and the two surface oxygens, thus increasing each v_{Al-O} by 0.2 v.u. Interestingly, the increase in the sum of bond valence incident to surface oxygens resulting from this displacement is similar to the difference of v_{Zn-O} between ^{IV}Zn and ^{VI}Zn (0.5 vs. 0.33 v.u.). Consequently, the occurrence of Al at an M2 site may promote the formation of the ^{VI}Zn complex.

4.2. Zn sorption at high $[Si]_{aq}$

4.2.1. Binding environment of Zn at high $[Si]_{aq}$

At high $[Si]_{aq}$, the detection of in-plane Zn–Zn pairs at 3.10(1) Å and of out-of-plane Zn–Si pairs at 3.30(2) Å supports the formation of Zn octahedral sheets that are parallel to montmorillonite platelets and connected to Si tetrahedral sheets. The incorporation of Zn in a phyllosilicate-like structural environment is further attested by the presence of a second Si shell at ~4.4–4.5 Å (peak C). Nearest Al cations were detected at 3.10 Å after 4 h of contact time, but no longer at 313 h. This result, together with the extremely low amount of aqueous Al, suggests that the Al shell corresponds to atoms exposed at the montmorillonite surface. This interpretation is consistent with the in-plane orientation of the Zn–Al pairs, and supports the epitaxial neoformation of a pure Zn hydrous layer silicate (i.e., Zn kerolite) in structural continuity to montmorillonite layers at 313 h of reaction time.

An estimate of the dimensions of the Zn domains can be obtained from the amount of Zn atoms in individual octahedral sheets (Q_{Zn}) and from $N_{Zn}^{35°}$ (Manceau and Calas, 1986; Schlegel et al., 2001b). For example, $N_{Zn}^{35°} = 1.2$ for HiSi-7-X4h (Table 3) is consistent with a mixture of 80% Zn dimers ($Q_{Zn} = 2$; $N_{Zn} = 1$) and 20% trimers ($Q_{Zn} = 3$; $N_{Zn} = 2$), or with 80% monomers ($Q_{Zn} = 1$; $N_{Zn} = 0$) and 20% large octahedral sheets ($Q_{Zn} \geqslant 200$; $N_{Zn} \approx 6$). Similarly, $N_{Zn}^{35°} = 3.4$ for HiSi-7-X313h can be obtained with 100% Zn sheets of 10–20 atoms, or 43% monomers and 57% large octahedral sheets. Consequently, the occurrence of small-sized surface Zn complexes can never be ruled out, even for long reaction times. In fact, some ^{IV}Zn complexes are still observed at $t = 313$ h and, because they are unlikely incorporated in the Zn octahedral sheets, they probably remain monomeric.

At $t = 4$ h, the small difference between the amounts of Zn sorbed at low and high $[Si]_{aq}$ (43 and 52 μmol Zn g^{-1}, respectively) precludes compelling coprecipitation of Zn and Si. Assuming that comparable amounts of monomeric Zn complexes formed at low and high $[Si]_{aq}$, then the amount of Zn in polymers is estimated to 52–43 = 9 μmol Zn g^{-1} (17% of sorbed Zn). In this extreme case, Zn polymers must be rather large (i.e., $Q_{Zn} > 200$) to account for $N_{Zn}^{35°} = 1.2(5)$ in HiSi-7-X4h. The same calculation performed from the amount of Zn-sorbed at low and high $[Si]_{aq}$ at $t = 168$ h (50 and 130 μmol Zn g^{-1}, respectively) suggests that the proportion of Zn monomers decreased from 43/52 = 83% to 50/130 = 38% of total Zn. The

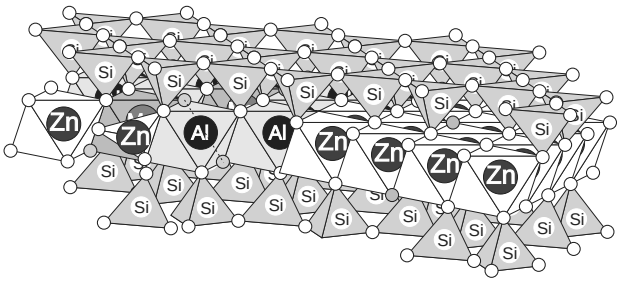

Fig. 11. Structural model for Zn sorption on montmorillonite at $[Si]_{aq} \sim 500$ μM and 313 h of reaction time (HiSi-7-X313h). In these conditions, Zn is distributed between Zn phyllosilicate domains and monomers.

assumed coexistence of large Zn sheets and ~38% monomeric Zn also results in a calculated $N_{Zn}^{35°}$ [(1–0.38) × 6 = 3.7, where 6 is the number of nearest Zn in an infinite layer] in agreement with experimental $N_{Zn}^{35°} = 3.4(5)$ value. The two independent calculations from solution chemistry and EXAFS support a bimodal size distribution of Zn surface complexes, represented by monomeric Zn complexes and by large-size ^{VI}Zn sheets.

In conclusion, EXAFS results collected at high $[Si]_{aq}$ indicate that Zn is progressively incorporated in Zn kerolite surface precipitates (Fig. 11). Since Zn kerolite contains only ^{VI}Zn, these precipitates likely nucleated from the monomeric ^{VI}Zn surface complexes. Therefore, the overall rate of Zn clay nucleation and growth is expected to be limited by the fractional amount of monomeric ^{VI}Zn surface complexes. This fraction, estimated from $N_{O_{1A}}^{35°}$ and $N_{O_{1B}}^{35°}$ for LoSi-7-X216 h (i.e., with Zn monomers only), equals [2.2(2)/6]/[4.0(3)/4+2.2(2)/6] = 27(3)% of total Zn, a relatively small value, which may account for the relatively slow rate of Zn-kerolite epitaxial growth on montmorillonite compared to hectorite.

4.2.2. Mechanism of Zn sorption at high $[Si]_{aq}$

The neoformed Zn kerolite is theoretically expected to have a Si/Zn ratio ⩽ 1.33, in contradiction to the Si/Zn ratio of 1.51(10) calculated from solution chemistry data. To lower the calculated ratio of Si to Zn uptake down to levels ⩽ 1.33, a "hidden" source of Zn must be invoked. This source may correspond to the desorption of Zn monomers, which formed in the first hours of the sorption experiments. This process seems realistic because kinetics measurements showed that near-equilibrium between aqueous Zn and monomeric Zn surface complexes was attained within 1 h, while the kinetics of clay formation proceeded at a much slower rate. To test this hypothesis, let us estimate the amount of monomeric Zn complexes as a function of time. This can be done by assuming that the formation of these complexes proceeds by a Langmuir-like reaction on a single type of sorption site ≡X:

$$\equiv X + Zn^{2+} \leftrightarrow \equiv XZn^{2+}, \quad (5)$$

where $\equiv XZn^{2+}$ is the surface complex. Assuming that the activity of surface species is nearly invariant upon metal loading, then the conditional equilibrium constant K^c equals

$$K^c = \frac{[\equiv XZn^{2+}]}{[\equiv X][Zn^{2+}]_{aq}}, \quad (6)$$

where $[\equiv X]$ and $[\equiv XZn^{2+}]$ stand for the concentrations of free and Zn-sorbed edge sites, respectively, and $[Zn^{2+}]_{aq} \approx [Zn]_{aq}$. Assigning the total concentration of edge sites (free and sorbed) to $[\equiv X]_{tot} = [\equiv X] + [\equiv XZn^{2+}]$ leads to the following relationship between solution and edge-sorbed Zn (Stumm and Morgan, 1996):

$$[\equiv XZn^{2+}] = \frac{[\equiv X]_{tot}[Zn^{2+}]_{aq}K^c}{1 + K^c[Zn^{2+}]_{aq}}, \quad (7)$$

from which $[\equiv XZn^{2+}]$ can be calculated at any time t, provided K^c and $[\equiv X]_{tot}$ are known. The value of $[\equiv X]_{tot}$ can be taken to be slightly greater than the maximal amount of monomeric Zn, e.g., ~54 μmol g^{-1}. The value of K^c, as calculated from $[Zn]_{aq}$, $[\equiv XZn^{2+}]$,

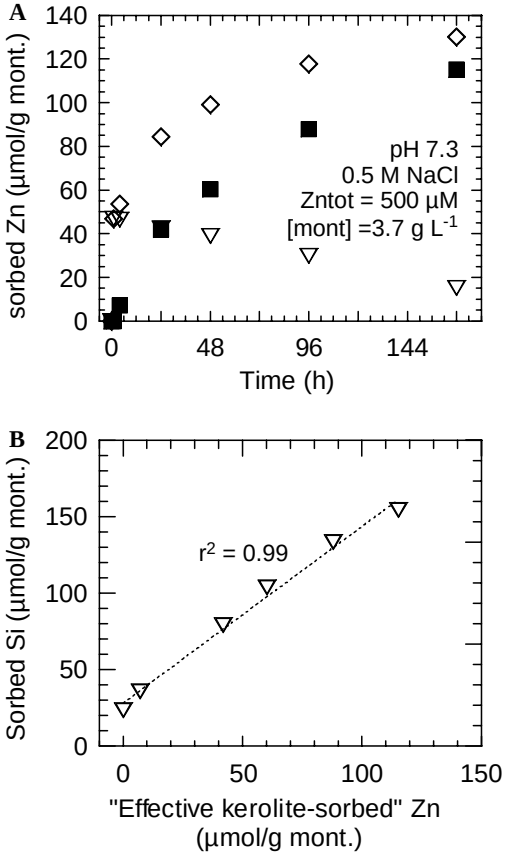

Fig. 12. (A) Kinetics of Zn sorption at $[Si]_{aq} \sim 500$ μM. (◇) Total amount of sorbed Zn. (▽) Amount of Zn monomers adsorbed on edge sites, assuming a total concentration of edge sites of 54 μmol g^{-1}. (■) Difference between the two previous quantities. (B) Correlation between the amounts of sorbed Si and Zn-sorbed in kerolite-like domains ("effective kerolite-sorbed" Zn). The latter quantity was calculated by subtracting the amount of monomeric Zn ($[\equiv XZn^{2+}]$) from the total amount of sorbed Zn. Regression slope of 1.15(13) (dotted line).

and $[\equiv X]_{tot}$ at $t = 1$ h in LoSi-7, equals $K^c = 1.82 \times 10^4$. Fig. 12A shows that the estimated amount of monomeric Zn ($[\equiv XZn^{2+}]$) decreased with time. Then, the amount of Zn incorporated in phyllosilicate (''effective kerolite-sorbed'' Zn in Fig. 12B) is obtained by subtracting $[\equiv XZn^{2+}]$ from the total (experimental) amount of sorbed Zn. The amount of ''effective kerolite-sorbed'' Zn varies linearly with sorbed Si (Fig. 12B), in a manner similar to the total amount of Zn-sorbed on montmorillonite (Fig. 4D). The slope of the new regression line (1.15(13)) now falls within the range of Si/Zn values for TO (Si/Zn = 0.67) and TOT (Si/Zn = 1.33) phyllosilicates. This agreement substantiates our hypothesis that Zn is transferred from monomeric sites to phyllosilicate nuclei upon time. The revised amount of monomeric Zn at the end of the experiment (15 μmol g^{-1}) is lower than the value (50 μmol g^{-1}) obtained by assuming that comparable amounts of monomeric Zn complexes formed at low and high $[Si]_{aq}$. The revised proportion of edge-sorbed monomeric Zn now equals 15/130 = 12%, a little low in comparison to the value derived from EXAFS data (43%). This difference suggests that the amount of edge-sorbed Zn, as calculated from Eq. (7), is probably underestimated.

4.2.3. Stability of Zn phyllosilicates

The constant Si/Zn uptake ratio for $t \geqslant 4$ h suggests that the octahedral and tetrahedral sheets of the neoformed phyllosilicate grow cooperatively at about the same rate. The formation of TO and TOT Zn phyllosilicate from dissolved species can be described by the following mass balance equations:

$$3Zn^{2+} + 2Si(OH)_4 + H_2O = Zn_3Si_2O_5(OH)_4 + 6H^+ \quad (8)$$

$$3Zn^{2+} + 4Si(OH)_4 = Zn_3Si_4O_{10}(OH)_2 + 6\ H^+ + 4H_2O \quad (9)$$

The clay formation decreases the solution supersaturation. This phenomenon can be quantified with the ion activity product (IAP), which is written for the reverse reactions of Eqs. (8) and (9):

$$IAP_{TO} = \frac{(Zn^{2+})^3(Si(OH)_4)^2}{(H^+)^6} \quad (10)$$

and

$$IAP_{TOT} = \frac{(Zn^{2+})^3(Si(OH)_4)^4}{(H^+)^6} \quad (11)$$

Assuming an ideal TOT composition, and using activity coefficients calculated from the Pitzer model (Chen and Marshall, 1982; Pitzer, 1987, 1991), IAP_{TOT} decreases from $\sim 10^{18.5(1.0)}$ at $t = 4$ h to $\sim 10^{13.9(1.0)}$ at $t = 313$ h. The IAP is expected to further decrease with reaction time, equaling the solubility constant of Zn kerolite at equilibrium. Therefore, the value calculated at $t = 313$ h is an upper limit for the solubility constant of Zn phyllosilicate. This experimental value agrees with that calculated previously ($K_{TOT} = 10^{8.5(5.9)}$; Manceau et al., 2000). The high IAP_{TOT} value at $t = 4$ h relative to K_{TOT} indicates that the initial suspension was highly supersaturated with respect to Zn kerolite, a condition required for the formation of stable nuclei (Stumm, 1992).

4.2.4. Comparison with previous results on phyllosilicate neoformation

The nucleation and epitaxial growth of Zn phyllosilicate described in this study can be compared to those reported for Ni phyllosilicate on montmorillonite. At pH 7.2, and for a lower concentration in Ni ($[Ni]_{total} = 20$ μM), it took about one year for Ni clay to nucleate and grow (Dähn et al., 2003). However, at pH 8.0 and $[Ni]_{total} = 660$ μm, Ni-phyllosilicate was observed by P-EXAFS spectroscopy after only two weeks, a timescale that compares well with that of our experiments (Dähn et al., 2002a). The relatively slow nucleation kinetics at pH 7.2 can be explained by the smaller degree of supersaturation.

Although comparable $[Zn]_{aq}$ and $[Si]_{aq}$ conditions were used in the present study and for Zn sorption on hectorite (Schlegel et al., 2001b), a difference in kinetics also was observed between these two systems, but in favor of the trioctahedral substrate. More Zn was incorporated in large-sized Zn domains ($Q_{Zn} > 200$) after 5 days of reaction with hectorite, than after 2 weeks with montmorillonite. This difference may stem from the structural similarities between Zn kerolite and hectorite, which decreases the interfacial energy between the clay sorbent and the sorbate nuclei. For montmorillonite, the interfacial energy between the dioctahedral substrate and the trioctahedral Zn kerolite, albeit still favoring nucleation, is probably more important, and thus stable nuclei ought to form at a slower rate.

Our results also shed new light onto the immobilization of Zn in contaminated soils and sediments. In these environments, high-content, and even pure, Zn phyllosilicate was identified by polarized and micro-EXAFS spectroscopy (Manceau et al., 2000; Isaure et al., 2005; Panfili et al., 2005). The present study shows that soil Al phyllosilicate, such as montmorillonite, and probably illite, which bears strong chemical and structural similarities with montmorillonite, may provide effective nucleation sites for Zn-containing phyllosilicate having a kerolite-like local structure. Formation of Zn phyllosilicate may also occur by homogeneous precipitation and aging of (Zn, Si) gels, e.g., upon soil drying. However, such gels are usually obtained in the laboratory at pH and concentrations in metal cations and silica much higher than in our experiments (Decarreau, 1981a, 1985). Consequently, the heteronucleation mechanism described here, occurring at lower IAP, is probably more relevant to natural systems. Also, clay particles obtained by homogeneous precipitation are completely disoriented and cannot be oriented for P-EXAFS experiments, in contrast to Zn-containing soil phyllosilicate. Consequently, the nucleation and growth of Zn-containing phyllosilicate at the edges of dioctahedral smectite crystallites explains well the observed anisotropy of the

Zn K-edge P-EXAFS signal from the clay fraction of contaminated soils and sediments. Finally, the period for clay heteronucleation and growth observed in our laboratory experiments (typically a few days) is short when compared to the timescale of soil contamination. Note, however, that kinetics observed in the laboratory may not apply directly to soil environments, due to obvious differences in chemistry (e.g., electrolyte composition, solid-solution ratio, temperature, and presence of organic molecules) that may impede or promote mineral (neo)formation.

5. Concluding remarks

The mechanism of Zn phyllosilicate nucleation and epitaxial growth previously documented on hectorite (Schlegel et al., 2001b) is now observed also on montmorillonite, a widespread and abundant soil and sediment constituent. Montmorillonite surfaces can provide nucleation sites for the neoformation of trioctahedral phyllosilicate, such as Zn kerolite, at $[Si]_{aq}$ typical of terrestrial systems and $[Zn]_{aq}$ found in contaminated environments. This uptake mechanism leads to Zn occlusion in a sparingly soluble phase in conditions where homogeneous precipitation is thermodynamically possible, but kinetically limited. The presence in contaminated soils and sediments of Zn-containing phyllosilicate having a trioctahedral Zn local structure is now well documented in the literature (see, e.g., Isaure et al., 2005; Panfili et al., 2005), and the present study helps to better understand the possible formation mechanism of these phases.

Acknowledgments

N. Geoffroy, J.L. Hazemann, O. Proux, and O. Ulrich, are thanked for their assistance during EXAFS measurements on FAME (ESRF). S. Chatain is thanked for her help for thermal analysis. We acknowledge K.L. Nagy and three anonymous reviewers for their constructive and thoughtful comments. This work was supported by the French-CRG program from CNRS and by DEN/DDIN/HAVL from CEA.

Associate editor: Kathyrn L. Nagy

References

Aberdam, D., 1998. SEDEM, a software package for EXAFS data extraction and modelling. *J. Synchrotron Rad.* **5**, 1287–1297.

Ankudinov, A.L., Rehr, J.J., 1997. Relativistic calculations of spin-dependent x-ray absorption spectra. *Phys. Rev. B* **56**, 1712–1715.

Baes, C.F.J., Mesmer, R.E., 1976. *The Hydrolysis of Cations*. John Wiley & Sons, New York.

Bickmore, B.R., Rosso, K.M., Nagy, K.L., Cygan, R.T., Tadanier, C.J., 2003. Ab initio determination of edge surface structures for dioctahedral 2:1 phyllosilicates: Implications for acid-base reactivity. *Clays Clay Miner.* **51**, 359–371.

Bleam, W.F., Welhouse, G.J., Janowiak, M.A., 1993. The surface coulomb energy and proton coulomb potentials of pyrophyllite {010}, {110}, {100}, and {130} edges. *Clays Clay Miner.* **41**, 507–516.

Brese, N.E., O'Keeffe, M., 1991. Bond-valence parameters for solids. *Acta Cryst.* **B47**, 192–197.

Brown, I.D., 1981. The bond-valence method: an empirical approach to chemical structure and bonding. In: O'Keefe, M., Navrotsky, A. (Eds.), *Structure and Bonding in Crystals. II*. Academic Press, New York, pp. 1–30.

Brown, I.D., 1992. Chemical and steric constraints in inorganic solids. *Acta Cryst.* **B48**, 553–572.

Chen, C.-T.A., Marshall, W.L., 1982. Amorphous silica solubility. IV. Behavior in pure water and aqueous sodium chloride, sodium sulfate, magnesium chloride, and magnesium sulfate solutions up to 350 °C. *Geochim. Cosmochim. Acta* **46**, 279–287.

Dähn, R., Scheidegger, A.M., Manceau, A., Schlegel, M.L., Baeyens, B., Bradbury, M.H., 2001. Ni clay neoformation on montmorillonite surface. *J. Synchrotron Rad.* **8**, 533–535.

Dähn, R., Scheidegger, A.M., Manceau, A., Schlegel, M.L., Baeyens, B., Bradbury, M.H., Morales, M., 2002a. Neoformation of Ni phyllosilicate upon Ni uptake by montmorillonite. A kinetics study by powder and polarized extended X-ray absorption fine structure spectroscopy. *Geochim. Cosmochim. Acta* **66**, 2335–2347.

Dähn, R., Scheidegger, A.M., Manceau, A., Curti, E., Baeyens, B., Bradbury, M.H., Chateigner, D., 2002b. Th uptake on montmorillonite: a powder and polarized extended X-ray absorption fine structure (EXAFS) study. *J. Colloid Interface Sci.* **249**, 8–21.

Dähn, R., Scheidegger, A.M., Manceau, A., Schlegel, M.L., Baeyens, B., Bradbury, M.H., Morales, M., 2003. Structural evidence for the sorption of metal ions on the edges of montmorillonite layers. A polarized EXAFS study. *Geochim. Cosmochim. Acta* **67**, 1–15.

Decarreau, A., 1981a. Cristallogenèse à basse température de smectites trioctaédriques par vieillissement de coprécipités silicométalliques de formule $(Si_{(4-x)}Al_x)M_3^{2+}O_{11}$, nH_2O, où x varie de 0 à 1 et où M^{2+} = Mg-Ni-Co-Zn-Fe-Cu-Mn. *C. R. Acad. Sci. Paris* **292**, 61–64.

Decarreau, A., 1981b. Mesure expérimentale des coefficients de partage solide/solution pour les éléments de transition A^{2+} dans les smectites magnésiennes (A = Ni, Co, Zn, Fe, Cu, Mn). *C. R. Acad. Sci. Paris* **292**, 459–462.

Decarreau, A., 1985. Partitioning of divalent transition elements between octahedral sheets of trioctahedral smectites and water. *Geochim. Cosmochim. Acta* **49**, 1537–1544.

Dietzel, M., 2000. Dissolution of silicates and the stability of polysilicic acid. *Geochim. Cosmochim. Acta* **64**, 3275–3281.

Drits, V.A., Besson, G., Muller, F., 1995. An improved model for structural transformations of heat-treated aluminous dioctahedral 2:1 layer silicates. *Clays Clay Miner.* **43**, 718–731.

Ford, R.G., Sparks, D.L., 2000. The nature of Zn precipitates formed in the presence of pyrophyllite. *Environ. Sci. Technol.* **34**, 2479–2483.

Grauby, O., 1993. Nature et étendue des solutions octaédriques argileuses. Approche par synthèse minérale. Ph.D., Université de Poitiers, Poitiers.

Grauby, O., Petit, S., Decarreau, A., Barronnet, A., 1993. The beidellite-saponite series: an experimental approach. *Eur. J. Miner.* **5**, 623–635.

Güven, N., 1988. Smectites. In: Bailey, S.W. (Ed.), *Hydrous Phyllosilicates*, Vol. 19. Mineralogical Society of America, Washington, DC, pp. 497–559.

Hazemann, J.-L., Nayouf, K., Debergevin, F., 1995. Modelization by finite-elements of sagittal focusing. *Nucl. Instrum. Methods Phys. Res. B* **97**, 547–550.

Iler, R.K., 1979. *The Chemistry of Silica*. John Wiley and Sons, New York.

Isaure, M.-P., Manceau, A., Geoffroy, N., Laboudigue, A., Tamura, N., Marcus, M.A., 2005. Zinc mobility and speciation in soil covered by contaminated dredged sediment using micrometer-scale and bulk-averaging X-ray fluorescence, absorption and diffraction techniques. *Geochim. Cosmochim. Acta* **69**, 1173–1198.

Kuzmin, A., Obst, S., Purans, J., 1997. X-ray absorption spectroscopy and molecular dynamics studies of Zn^{2+} hydration in aqueous solutions. *J. Phys.-Condens. Matter* **9**, 10065–10078.

Lee, S., Anderson, P.R., Bunker, G.B., Karanfil, C., 2004. EXAFS study of Zn sorption mechanisms on montmorillonite. *Environ. Sci. Technol.* **38**, 5426–5432.

Manceau, A., Calas, G., 1986. Nickel-bearing clay minerals: II. Intracrystalline distribution of nickel: an X-ray absorption study. *Clay Miner.* **21**, 341–360.

Manceau, A., Combes, J.-M., 1988. Structure of Mn and Fe oxides and oxyhydroxides: a topological approach by EXAFS. *Phys. Chem. Miner.* **15**, 283–295.

Manceau, A., Chateigner, D., Gates, W.P., 1998. Polarized EXAFS, distance-valence least-squares modeling (DVLS) and quantitative texture analysis approaches to the structural refinement of Garfield nontronite. *Phys. Chem. Miner.* **25**, 347–365.

Manceau, A., Marcus, M.A., Tamura, N., 2002a. Quantitative speciations of heavy metals in soils and sediments by synchrotron X-ray techniques. In: Fenter, P.A., Rivers, M.L., Sturchio, N.C., Sutton, S.R. (Eds.), *Applications of Synchrotron Radiation in Low-Temperature Geochemistry and Environmental Science*, Vol. 49. Mineralogical Society of America and Geochemical Society, Washington, DC, pp. 341–428.

Manceau, A., Lanson, B., Drits, V.A., 2002b. Structure of heavy metal sorbed birnessite. Part III: results from powder and polarized extended X-ray absorption fine structure spectroscopy. *Geochim. Cosmochim. Acta* **66**, 2639–2663.

Manceau, A., Bonnin, D., Kaiser, P., Fretigny, P., 1988. Polarized EXAFS of biotite and chlorite. *Phys. Chem. Miner.* **16**, 180–185.

Manceau, A., Bonnin, D., Stone, W.E.E., Sanz, J., 1990. Distribution of Fe in the octahedral sheet of trioctahedral micas by polarized EXAFS. Comparison with NMR results. *Phys. Chem. Miner.* **17**, 363–370.

Manceau, A., Marcus, M.A., Tamura, N., Proux, O., Geoffroy, N., Lanson, B., 2004. Natural speciation of Zn at the micrometer scale in a clayey soil using X-ray fluorescence, absorption, and diffraction. *Geochim. Cosmochim. Acta* **68**, 2467–2483.

Manceau, A., Boisset, M.C., Sarret, G., Hazemann, R.L., Mench, M., Cambier, P., Prost, R., 1996. Direct determination of lead speciation in contaminated soils by EXAFS spectroscopy. *Environ. Sci. Technol.* **30**, 1540–1552.

Manceau, A., Tamura, N., Celestre, R.S., MacDowell, A.A., Geoffroy, N., Sposito, G., Padmore, H.A., 2003. Molecular-scale speciation of Zn and Ni in soil ferromanganese nodules from loess soils of the Mississippi Basin. *Environ. Sci. Technol.* **37**, 75–80.

Manceau, A., Lanson, B., Schlegel, M.L., Hargé, J.-C., Musso, M., Hazemann, J.-L., Chateigner, D., Lamble, G.M., 2000. Quantitative Zn speciation in smelter-contaminated soils by EXAFS spectroscopy. *Am. J. Sci.* **300**, 289–343.

Manceau, A., Tommaseo, C., Rihs, S., Geoffroy, N., Chateigner, D., Schlegel, M., Tisserand, D., Marcus, M.A., Tamura, N., Chen, Z.-S., 2005. Natural speciation of Mn, Ni and Zn at the micrometer scale in a clayey paddy soil using X-ray fluorescence, absorption, and diffraction. *Geochim. Cosmochim. Acta*.

Marcus, M.A., Manceau, A., Kersten, M., 2004. Mn, Fe, Zn and As speciation in a fast-growing ferromanganese marine nodule. *Geochim. Cosmochim. Acta* **68**, 3125–3136.

Morin, G., Ostergren, J.D., Juillot, F., Ildefonse, P., Calas, G., Brown Jr., G.E., 1999. XAFS determination of the chemical form of lead in smelter-contaminated soils and mine tailings: Importance of adsorption processes. *Am. Miner.* **84**, 420–434.

Newville, M., 2001. EXAFS analysis using FEFF and FEFFIT. *J. Synchrotron Rad.* **8**, 96–100.

Newville, M., Livins, P., Yacoby, Y., Rehr, J.J., Stern, E.A., 1993. Near-edge X-ray absorption fine structure of Pb: a comparison of theory and experiment. *Phys. Rev. B* **47**, 14126–14131.

Panfili, F., Manceau, A., Sarret, G., Spadini, L., Kirpichtchikova, T., Bert, V., Laboudigue, A., Marcus, M.A., Ahamdach, N., Libert, M.F., 2005. The effect of phytostabilization on Zn speciation in a dredged contaminated sediment using scanning electron microscopy, X-ray fluorescence, EXAFS spectroscopy and principal components analysis. *Geochim. Cosmochim. Acta* **69**, 2265–2284.

Pitzer, K.S., 1987. A thermodynamic model for aqueous solutions in liquid-like density. In: Carmichael, I.S.E., Eugster, H.P. (Eds.), *Thermodynamic Modeling of Geological Materials: Minerals, Fluids and Melts*, Vol. 17. Mineralogical Society of America, Washington, DC, pp. 97–142.

Pitzer, K.S., 1991. Ion interaction approach: theory and data correlation. In: Pitzer, K.S. (Ed.), *Electrolytic Solutions*. CRC Press, Boca Raton, FL, pp. 75–154.

Ravel, B., Newville, M., 2005. ATHENA, ARTEMIS, HEPHAESTUS: data analysis for X-ray absorption spectroscopy using IFEFFIT. *J. Synchrotron Rad.* **12**, 537–541.

Roberts, D.R., Ford, R.G., Sparks, D.L., 2003. Kinetics and mechanisms of Zn complexation on metal oxides using EXAFS spectroscopy. *J. Colloid Interface Sci.* **263**, 364–376.

Ross, C.S., 1946. Sauconite—a clay mineral of the montmorillonite group. *Am. Miner.* **31**, 411–424.

Sarret, G., Manceau, A., Spadini, L., Roux, J.C., Hazemann, J.-L., Soldo, Y., Eybert-Berard, L., Menthonnex, J.-J., 1998. Structural determination of Zn and Pb binding sites in *Penicillium chrysogenum* cell walls by EXAFS spectroscopy. *Environ. Sci. Technol.* **32**, 1648–1655.

Scheidegger, A.M., Lamble, G.M., Sparks, D.L., 1996. Investigation of Ni adsorption on pyrophyllite: an XAFS study. *Environ. Sci. Technol.* **30**, 548–554.

Scheidegger, A.M., Lamble, G.M., Sparks, D.L., 1997. Spectroscopic evidence for the formation of mixed-cation hydroxide phases upon metal sorption on clay and aluminium oxides. *J. Colloid Interface Sci.* **186**, 118–128.

Scheinost, A.C., Kretzschmar, R., Pfister, S., 2002. Combining selective sequential extractions, x-ray absorption spectroscopy, and principal component analysis for quantitative zinc speciation in soil. *Environ. Sci. Technol.* **36**, 5021–5028.

Schlegel, M.L., Charlet, L., Manceau, A., 1999a. Sorption of metal ions on clay minerals. II. Mechanism of Co sorption on hectorite at high and low ionic strength, and impact on the sorbent stability. *J. Colloid Interface Sci.* **220**, 392–405.

Schlegel, M.L., Manceau, A., Chateigner, D., Charlet, L., 1999b. Sorption of metal ions on clay minerals. I. Polarized EXAFS evidence for the adsorption of cobalt on the edges of hectorite particles. *J. Colloid Interface Sci.* **215**, 140–158.

Schlegel, M.L., Manceau, A., Hazemann, J.-L., Charlet, L., 2001a. Adsorption mechanisms of Zn on hectorite as a function of time, pH, and ionic strength. *Am. J. Sci.* **301**, 798–830.

Schlegel, M.L., Manceau, A., Charlet, L., Chateigner, D., Hazemann, J.-L., 2001b. Sorption of metal ions on clay minerals. III. Nucleation and epitaxial growth of Zn phyllosilicate on the edges of hectorite. *Geochim. Cosmochim. Acta* **65**, 4155–4170.

Shannon, R.D., 1976. Revised effective ionic radii and systematic studies of interatomic distances in halides and chalcogenides. *Acta Cryst.* **A32**, 751–767.

Stumm, W., 1992. *Chemistry of the Solid-Water Interface*. John Wiley & Sons, New York.

Stumm, W., Morgan, J.J., 1996. *Aquatic Chemistry*. John Wiley & Sons, New York.

Teo, B.K., 1986. *EXAFS: Basic Principles and Data Analysis*. Springer-Verlag, Berlin.

Tournassat, C., Greneche, J.M., Tisserand, D., Charlet, L., 2004. The titration of clay minerals I. Discontinuous backtitration technique combined with CEC measurements. *J. Colloid Interface Sci.* **273**, 224–233.

Tournassat, C., Neaman, A., Villieras, F., Bosbach, D., Charlet, L., 2003. Nanomorphology of montmorillonite particles: estimation of the clay edge sorption site density by low-pressure gas adsorption and AFM observations. *Am. Miner.* **88**, 1989–1995.

Trainor, T.P., Brown Jr., G.E., Parks, G.A., 2000. Adsorption and precipitation of aqueous Zn(II) on alumina powders. *J. Colloid Interface Sci.* **231**, 359–372.

Tsipursky, S.I., Drits, V.A., 1984. The distribution of octahedral cations in the 2:1 layers of dioctahedral smectites studied by oblique-texture electron diffraction. *Clay Miner.* **19**, 177–193.

Waychunas, G.A., Fuller, C.C., Davis, J.A., 2002. Surface complexation and precipitate geometry for aqueous Zn(II) sorption on ferrihydrite:

I. X-ray absorption extended fine structure analysis. *Geochim. Cosmochim. Acta* **66**, 1119–1137.

Webb, S.M., Leppard, G.G., Gaillard, J.-F., 2000. Zinc speciation in a contaminated aquatic environment: characterization of environmental particles by analytical electron microscopy. *Environ. Sci. Technol.* **34**, 1926–1933.

White, G.N., Zelazny, L.W., 1988. Analysis and implication of the edge structure of dioctaedral phylosilicates. *Clays Clay Miner.* **36**, 141–146.